(A New Letter-Of-Intent to Jefferson Lab PAC-29)

First Measurement of Polarized EMC Effect for the Neutron

December 5, 2005

X. Zheng[1]
Argonne National Laboratory, Argonne, IL 60439

A. Deur[2]
Jefferson Lab, Newport News, VA 23606

Abstract

We propose to measure the EMC effect in polarized structure function for the neutron g_{1n} at $x = 0.19$ using a polarized ^{3}He and a polarized ^{129}Xe targets in Hall A. Results of this measurement would provide the first data on polarized EMC effect and important information for our understanding of the medium modification of nucleon spin structure.

In this document, we first review the history and theories of the unpolarized EMC effect, and present existing calculations on the polarized EMC effect. Experimental design of the proposed measurement is presented in section 2 and a possible design for the new polarized Xe target is described in section 3. Extractions of g_{1n} from He and Xe data are discussed in section 4. An analysis of all systematic and theoretical uncertainties is given in section 5. In section 6 we give the kinematics optimization and estimation of rates and statistical uncertainties for a polarized EMC measurement. We will then discuss possible physics impact and summarize the beam time request. Although we propose to use ^{129}Xe, we will show that ^{21}Ne is another possible nuclear target to use, which although requires more R&D effort, may provide similar or better statistical precision.

Contents

---

[1]Email: xiaochao@jlab.org
[2]Email: deurpam@jlab.org

1 The EMC Effect

1.1 Unpolarized EMC Effect – Data and Theories

In 1982, the European Muon Collaboration (EMC) used nuclear targets in muon scattering to measure structure functions. The initial goal of using nuclear targets was to increase luminosity, and it was expected that nuclear effects would only be seen at low x where nuclear shadowing occurs and as $x \to 1$ where additional smearing from nuclear Fermi motion is present. But the results on the nuclear to nucleon structure function ratio, defined as $R^A(x) \equiv F_2^A(x)/F_2^D(x)$ where F_2^A is the structure function of a nuclear target with mass number A and F_2^D is the deuteron structure function, show that $R^A(x)$ was significantly less than 1 in the range of $0.3 < x < 0.8$ [1]. This phenomenon, refereed to as the EMC effect, triggered extensive studies on nuclear structure functions in the past 20 years. Experimentally, measurements using nuclear targets have been made by the EMC, BCDMS, SLAC, E665 and NMC collaborations. Their data covered a wide kinematic range within $10^{-4} < x < 0.9$ and $0.8 < Q^2 < 70$ (GeV)^2, and included various nuclear targets such as ^{4}He, ^{9}Be, ^{27}Al, ^{56}Fe, ^{65}Cu, ^{129}Xe and ^{197}Au. Recently, EMC effect on light nuclei ^{3}He and ^{4}He have been performed at Jefferson Lab [3].

Theoretically, people have been strived to understand the EMC effect. A full understanding of the EMC effect may require an accurate description of many quark system in the framework of quantum chromo-dynamics (QCD), which is probably difficult to achieve in the near future. For now one can only explain this effect from models, for example, nuclear shadowing and anti-shadowing, dynamical rescaling, Nambu-Jona-Lasinio (NJL) model, chiral quark model, *etc.*. However, although these models can more or less explain the data in a particular x region, none of them works for the full region from $x = 0$ to 1. On the other hand, understanding fully the EMC effect is crucial in developing a QCD prescription to describe the nucleus at the partonic level.

An overview of measurements and models of the EMC effect can be found in Ref. [4]. In the following we describe briefly a phenomenological study which has been widely used by the community. A convenient way to quantify the EMC effect is to study the x- and the A-dependencies of $R^A(x)$. In an attempt to quantify EMC effect for all nuclear targets, the ratios $R^A(x)$ from world data were combined and fit with a function linear in $A^{-1/3}$, which was then extrapolated to infinite nuclear mass $A \to \infty$ [5]. Their results are shown in Fig. 1. Also although it is known that the structure function evolves as Q^2, $R^A(x)$ is observed to be nearly Q^2-independent. From Fig. 1 one can deduce the unpolarized EMC effect for any nuclear target by scaling the difference between unity and the EMC ratio of nuclear matter by $(1 - (\frac{A}{2})^{-1/3})$, *i. e.* scaling by a factor of 0.13 for ^{3}He, 0.34 for ^{7}Li, 0.54 for ^{21}Ne and 0.75 for ^{129}Xe.

1.2 Theories for Polarized EMC Effect

Compared to unpolarized sector, the polarized counterpart of EMC effect is poorly explored: The first discussion of polarized EMC effect was in the context of dynamical rescaling [6]. Since then there exist only a handful of predictions on the polarized EMC ratio. And although polarized data on light nuclei such as ^{2}D, ^{3}He or ^{6}Li exist, no dedicated experiment on the polarized EMC ratio has been performed yet. We describe below available predictions.

At small x, calculations using nuclear shadowing and nuclear enhancement show about $20(55)\%$ effect for $g_{1,A=7}^{n.s.}(x,Q^2)/g_{1N}^{n.s.}(x,Q^2)$ and $14(40)\%$ effect for $g_{1,A=3}^{n.s.}(x,Q^2)/g_{1N}^{n.s.}(x,Q^2)$ at $x =$

Figure 1: Extrapolation from nuclear target data to nuclear matter $A^{-1/3} = 0$ (left) and the extracted nuclear matter to deuteron ratio *vs.* x (right) [5]. The error bars shown include both statistical and systematical errors of world data.
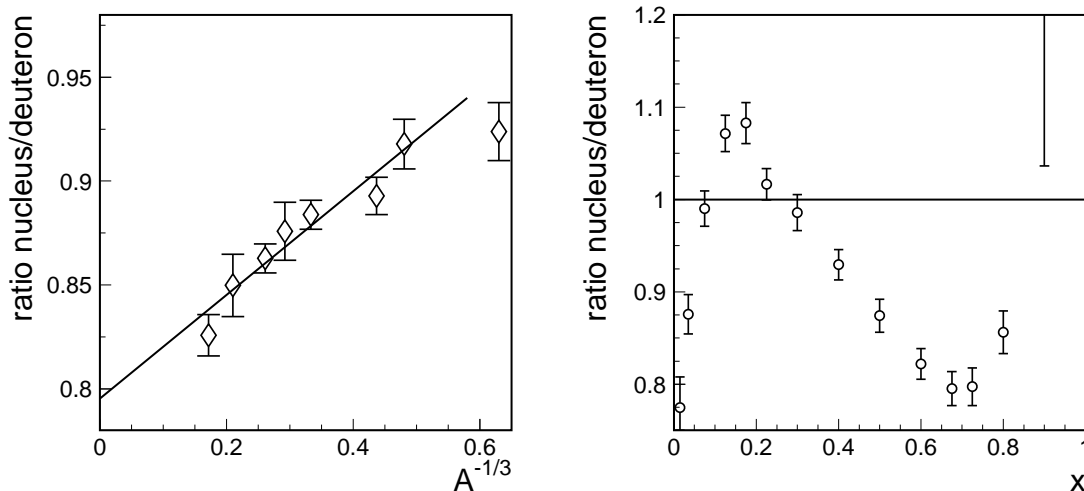
$0.125(0.15)$ [7, 8]. Here $g_{1,A=3}^{n.s.}(x,Q^2) = g_1^{^3\mathrm{H}} - g_1^{^3\mathrm{He}}$ and $g_{1,A=7}^{n.s.}(x,Q^2) = g_1^{^7\mathrm{Li}} - g_1^{^7\mathrm{B}}$. If using a naive expectation that the nuclear effect scales as $1 - A^{-1/3}$ analogous to its unpolarized counterpart(except that we are using A instead of $A/2$ because the "reference" free nucleon structure function is for $A = 1$ now), we find a $\approx 45\%(120\%)$ effect for $g_{1,A\to\infty}^{n.s.}/g^{n.s.}$ at $x = 0.125(0.15)$.

A more recent calculation using a modified Nambu-Jona-Lasinio model suggests a large polarized EMC effect at all x [9]. EMC effect on the valence quark spin distribution is calculated at $Q^2 = 0.16$ (GeV)^2 and evolved to higher Q^2 to give the EMC ratio for full (both valence and sea) quark distributions, where sea quarks are generated through Q^2 evolution. The EMC ratio on the proton g_{1p}^A/g_{1p} is found to be $(20-30)\%$ below unity for a wide range of $0 < x < 0.8$, as shown by the lower curve on the left panel of Fig. 2. This is about twice the size of the unpolarized EMC effect. In particular, in region $x < 0.2$ the polarized proton EMC ratio stays at 0.8, while the unpolarized EMC ratio rises above 1 because of nuclear shadowing and enhancement effects. Shown on the right panel of Fig. 2 are the EMC ratios of quark spin distributions $(\Delta u + \Delta \bar{u})$ and $(\Delta d + \Delta \bar{d})$ at $Q^2 = 10$ (GeV)^2 from the same model. It is expected in this model that the Q^2-dependence of the EMC ratio is small.

Another recent calculation [10] is from the chiral quark-soliton model, which predicts also a sizable effect for the isovector component $g_1^p - g_1^n$ at the order of $\bigcirc(N_C)$. The effect for the isoscalar component, $g_1^p + g_1^n$, on the other hand, is of the order of $\bigcirc(1)$ and is much smaller than the isovector component. The x-dependence and the size of ratio $R_1(x) \equiv (g_1^{p,A} - g_1^{n,A})/(g_1^p - g_1^n)$ are calculated and are found to be quite similar to the unpolarized EMC ratio, as shown by the full calculation (solid curve) in Fig. 3. It has a similar rising as Ref. [7, 8] in the small x region. And the valence quark calculation from this model (dashed curve) is similar to Ref. [9].

Figure 2: Predictions from the NJL model [9]. Left: Ratios of the unpolarized and polarized nuclear to nucleon structure functions at nuclear matter density. The top curve is F_2^A/F_2^D compared to world data [5]. The bottom curve is for the proton g_{1p}^A/g_{1p}. Right: Ratio of quark spin distributions in nuclear matter to the corresponding free distributions at a scale of $Q^2 = 10$ (GeV)^2. The solid line is for $\Delta u^A(x)/\Delta u(x)$ and dot-dashed line is for $\Delta d^A(x)/\Delta d(x)$.
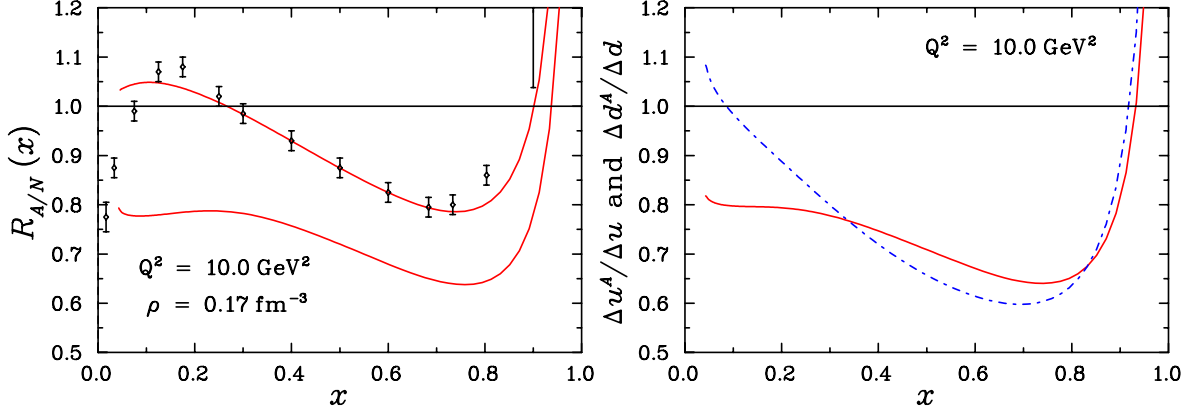
Figure 3: Ratio for the quark spin distributions in nuclear matter to the corresponding free distributions in the chiral quark model [10]. The solid curve is for the ratio at $Q^2 = 10$ (GeV)^2 and (red) dotted curve is for $Q^2 = 1$ (GeV)^2. The (blue) dashed curve shows the ratio for valence quarks.
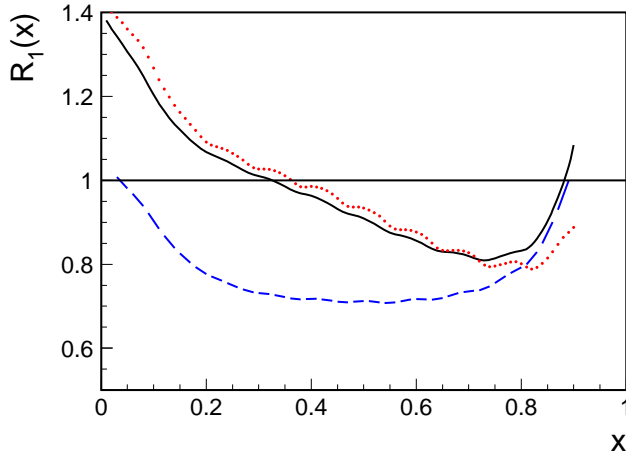
1.3   Polarized EMC Effect on the Neutron

We use Ref. [9] and Ref. [10] to estimate the EMC effect on the neutron polarized structure functions, g_1^n and g_2^n. We first calculate the free nucleon value using world fits of polarized parton distribution functions (PDF) [11, 12, 13, 14] and $g_{1N} = \sum e_i^2 [\Delta q_{i,fit}(x)]$. For Ref. [9], we correct the free nucleon PDF Δq by the calculated $\Delta q^A/\Delta q$ (right panel of Fig. 2). In doing so we have assumed these ratios have little Q^2-dependence as in the unpolarized case. Then we construct the in-medium nucleon structure functions g_{1N}^A using $g_{1N}^A = \sum e_i^2 [\Delta q_{i,fit}(x) \Delta q^A/\Delta q]$. The nuclear corrections in Ref. [10] are given for the isovector component $g_{1p} - g_{1n}$ and it was claimed the cor-

Figure 4: EMC effect on g_1^n and g_2^n. The free nucleon calculations (blue) are based on world characterizations of polarized PDFs. The in-medium nucleon calculations are based on Ref. [9] (g_{1n}^A (valence), red) and Ref. [10] (g_{1n}^A, green).
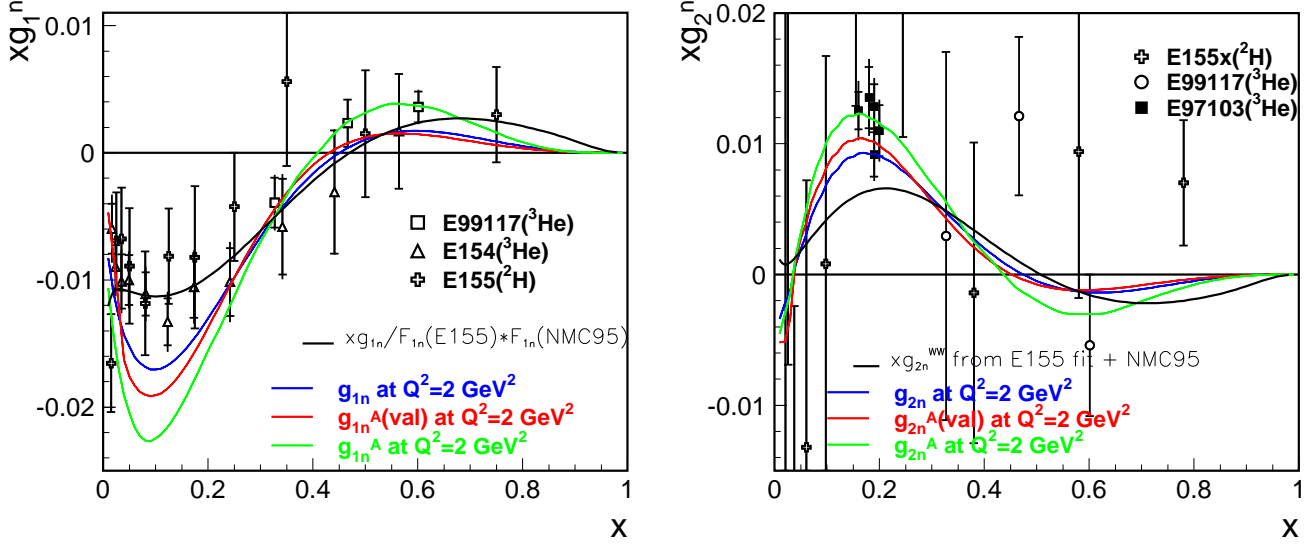
rections for the isoscalar component are relatively small. Therefore we take the EMC ratio R_{emc} for the from Fig. 3 and correct only the isovector free nucleon structure functions, then construct g_{1N}^A from the isovector (medium modification applied) and the isoscalar (medium modification negligible) components. The results are shown in Fig. 4. The values of structure function g_2 are calculated using $g_{1p,n}$ and $g_{1p,n}^A$ and the Wandzura-Wilczek relation [15]:

$$g_2^{WW}(x, Q^2) = -g_1(x, Q^2) + \int_x^1 \frac{g_1(y, Q^2)}{y} \mathrm{d}y \,. \tag{1}$$

2 Experimental Setup

2.1 Overview

The floor plan for Hall A is shown in Fig 5. We use a polarized ^{3}He cell and an identically shaped polarized ^{129}Xe cell for the measurement of free and in-medium neutron spin structure function, respectively. The maximum beam currents are $15~\mu$A for ^{3}He and $30~\mu$A for ^{129}Xe. The scattered electrons are detected by the two standard Hall A High Resolution Spectrometers (HRS) [16]. A fast Data Acquisition (DAQ) system currently being built by the PVDIS collaboration [17] will be used to accommodate the high rate from the Xe target. The regular HRS DAQ will be used to cross check the results for rates below 4 KHz. A Luminosity Monitor (Lumi) is located downstream on the beam-line to monitor the helicity dependent beam asymmetries and all possible false asymmetries to the 10^{-7} level. In this chapter we will describe briefly the beam polarimetry, the spectrometers and the DAQ.

Figure 5: Hall A floor plan for the proposed measurement.
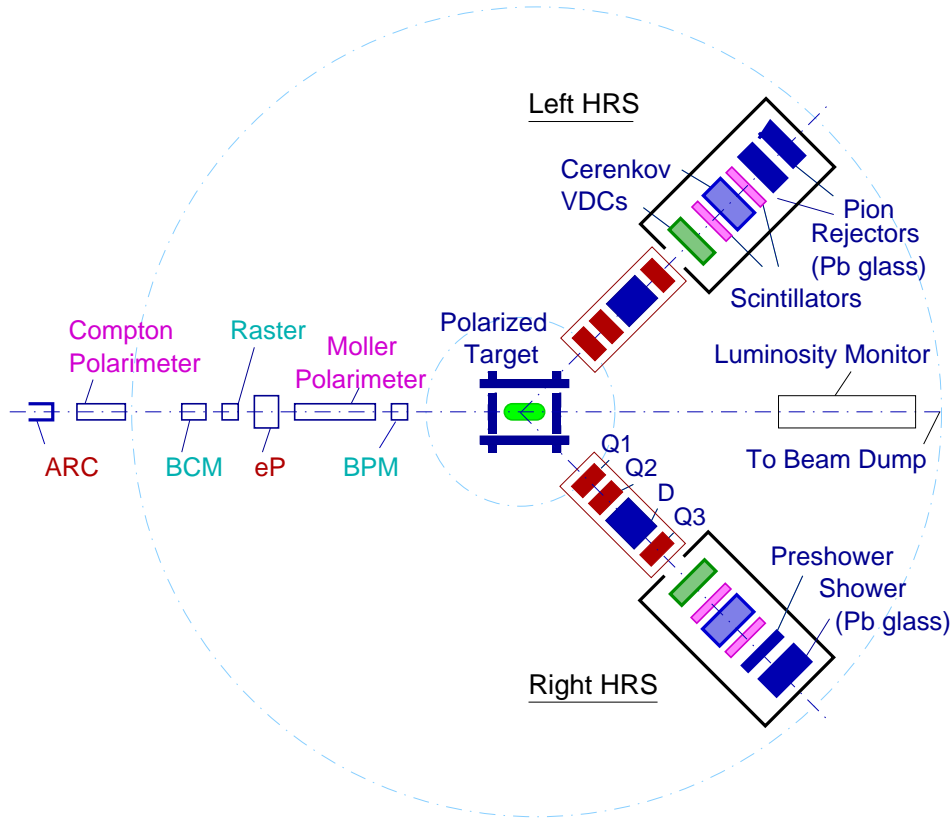
2.2 Beam line and beam quality control

We propose to use 6.0 GeV polarized beam with a 80% polarization. The maximum beam current is 30 μA. To reduce the heat impact on the target, the beam is circularly rastered such that the beam spot size at the target is ≈ 4 mm in diameter. The beam energy can be measured to a $\Delta E/E = 2 \times 10^{-4}$ level using the ARC device [16]. We need the standard Compton and Moller polarimeters to measure the beam polarization. Presently the Moller polarimeter typically provide a precision of $\Delta P_b/P_b = 3\%$ which is sufficient for the proposed measurement. The Compton polarimeter will be upgraded to a green laser within next couple of years in preparation for the PVDIS [17] and the Pb-parity experiments [18]. The green Compton is expected to provide a 1% precision for 6 GeV beam and we will use it for the proposed measurement if available.

Due to the small size of the expected measured asymmetries, especially for the polarized Xe target, we need parity-quality beam for the proposed measurement. This includes utilizing the well developed parity DAQ to control beam helicity asymmetry and the luminosity monitor to control false asymmetry and any helicity-correlated effects. The beam helicity asymmetry was controlled to the 10^{-7} level and the false asymmetry was monitored to be ~ 10 ppb during the 2005 run of HAPPEX-He and HAPPEX-H [20]. These are more than enough for the proposed measurement.

2.3 Spectrometers and the fast counting DAQ

We will use the standard Hall A High Resolution Spectrometer (HRS). For each HRS the effective solid angle acceptance for an extended target is 5.4 msr and the momentum bite is $\pm 4.5\%$. The central momentum of the HRS can be calculated from the dipole field magnitude and the HRS constant to the 5×10^{-4} level [21]. The HRS central angle can be determined to ± 0.2 mrad using $H(e, e'p)$ elastic scattering data with careful analysis [22]. The maximum momentum is 4 GeV/c for the left HRS and 3.1 GeV/c for the right HRS.

For inelastic scattering measurements, one must separate scattered electrons cleanly from photo- and electro-produced pion background. For this purpose, each HRS is equipped with a CO_2 Čerenkov detector and a double-layered lead glass shower detector. Using data from past experiments with < 1 KHz event rate, the combined pion rejection factor of these two detectors was found to be $\geq 10^4$ [23] while keeping a $> 99\%$ electron detection efficiency for each. At high rate, a practical estimate of the PID efficiency should also take into account the effect of event pileup, detector readout deadtime and electronic noise. We plan to use a fast counting flash ADC-based DAQ for the proposed measurement. This new DAQ system is expected to handle up to 1 MHz events rate with a $\geq 10^3$ on-board pion rejection efficiency and a $< 0.3\%$ uncertainty in deadtime corrections, which are sufficient for the proposed measurement. It is currently being built by the PVDIS collaboration [17] and is expected to be ready in fall of 2007.

3 Polarized Gas Target

Polarized ^{3}He target has been routinely used in Hall A for neutron spin structure study. A typical ^{3}He cell has a pressure of $(11 - 12)$ atm under running conditions, can take up to $15\ \mu$A beam and maintain a 40% in-beam polarization. In this section we focus mainly on a polarized ^{129}Xe cell, a new instrument needed for the proposed measurement. The same technique can in principle be used to polarized ^{21}Ne although more polarizing technique is required in addition to the new cell design.

3.1 Choice of Noble Gases

To choose a nuclear target for polarized DIS experiment, various factors need to be taken into account:

- whether the nucleus has a non-zero spin;
- whether the technique to polarized it is mature;
- whether the isotope is stable and easy to obtain;
- An s-shell for the unpaired nucleon is preferred so that the effective nucleon polarization is high;
- A spin $1/2$ is preferred so that tensor polarizations do not need to be disentangled from the measurement.

We list in table 1 properties of all noble gas nuclei that might be polarized using optical pumping technique and spin-exchange with alkaline vapor. One can see that only a few noble gas isotopes have non-zero spin and are stable: ^{3}He, ^{21}Ne, ^{83}Kr, ^{129}Xe and ^{131}Xe. In addition when the unpaired nucleon has large angular momentum, the spin of the nuclei comes mostly from angular momentum of nucleons, not the nucleon spin. For example one set of shell model calculations shows that the unpaired neutron in ^{21}Ne is only 58% polarized and the rest of ^{21}Ne's spin comes from protons' angular momentum $L(p) = 0.233$ and spin $S(p) = 0.011 = 0.022 \times \frac{1}{2}$ and the neutron's angular momentum $L(n) = 0.964$ [24]. Another set of shell model calculations give similar results for ^{21}Ne: $S_n = 0.29 = 0.58 \times \frac{1}{2}$, $S_p = 0.01$, $L_n = 0.96$, $L_p = 0.23$; for ^{83}Kr $S_n = 0.47$, $S_p = 0.01$, $L_n = 3.75$ and $L_p = 0.26$; and for ^{129}Xe, using a basis dimension of three billion, $S_n = 0.362$, $S_p = 0.008$, $L_n = 0.053$, $L_p = 0.077$ [25]. Another advantage to use spin $1/2$ nuclei is that one does not need to deal with tensor polarizations.

All noble gas nuclei with non-zero spin can be polarized in the same principles as ^{3}He: optical pumping of alkaline vapor (usually Rb) atoms followed by spin-exchange between Rb and the noble gas nucleus. However ^{131}Xe has large spin destruction rate due to coupling between collision-induced Xe-Xe diatomic molecule's electric quadrupole interaction between nuclear spin and rotational angular momenta [29], which makes the spin polarization of ^{131}Xe nearly useless. ^{21}Ne gas has also been polarized but its polarizing mechanism was not studied as extensively as Xe and ^{3}He because of its lower potential in medical physics applications. ^{129}Xe has much smaller spin destruction rate because only dipole relaxation is present in Xe-Xe collision. Techniques to polarize ^{129}Xe gas has been studied extensively and hyper-polarized ^{129}Xe gas has been used readily at various institutions for medical physics purposes such as nuclear magnetic resonance

imaging (MRI). A large effort, supported by solid funding, is currently underway in medical imaging physics to develop high ^{129}Xe polarization. It is now timely to apply these development to experimental nuclear physics.

Because of the reasons stated above, we choose to use isotope ^{129}Xe in this document. However, as we will explain in details later, measurement of polarization observables using heavy target is difficult because of both large dilution from the $A - 1$ unpolarized nucleons in the target and the uncertainty in nuclear corrections. Thus in this section we also give characteristics of ^{21}Ne to study its potential of being used as a polarized target.

Table 1: Properties of noble gas nuclei relevant to polarized gas target design.

Z	Isotope	spin	Abundance	μ (in μ_N)	shell of unpaired neutron	polarized before?
2	^{3}He	1/2	0.000138%	-2.12762	1s	Yes, widely used
	^{4}He	0	99.999862%	–	–	–
10	^{20}Ne	0	90.48%	–	–	–
	^{21}Ne	3/2	0.27%	-0.66179	1d	Yes, in research only
18	^{36}Ar	0	0.34%	–	–	–
	^{38}Ar	0	0.06%	–	–	–
	^{40}Ar	0	99.6%	–	–	–
36	^{78}Kr	0	0.35%	–	–	–
	^{80}Kr	0	2.25%	–	–	–
	^{82}Kr	0	11.6%	–	–	–
	^{83}Kr	9/2	11.5%	-0.970	1g	No(?)
	^{84}Kr	0	57.0%	–	–	–
	^{86}Kr	0	17.3%	–	–	–
54	^{128}Xe	0	1.91%	–	–	–
	^{129}Xe	1/2	26.4%	-0.7768	3s	Yes, widely used
	^{130}Xe	0	4.1%	–	–	–
	^{131}Xe	3/2	21.2%	?	2d(?)	Yes, in research only
	^{132}Xe	0	26.9%	–	–	–
	^{134}Xe	0	10.4%	–	–	–
	^{136}Xe	0	8.9%	–	–	–
86	^{219}Rn	5/2	Trace†	?	–	–
	^{220}Rn	0	Trace†	–	–	–
	^{222}Rn	0	Trace†	–	–	–

† radioactive

3.2 New target design

The basic principle of a typical polarized gas target used at SLAC and JLab is described in Appendix A. For a standard two-chamber cell design, polarization of the noble gas in the target chamber is determined by several factors including laser pumping power, laser linewidth, density

of the Rb vapor, cell geometry, cell fill density, material of the cell glass wall and coating, and diffusion of the polarized gas from the pumping chamber to target chamber. In Appendix A we analyze the possible polarization of Xe gas for a two-chamber cell. We found that this traditional design is not suitable for Xe because of two reasons:

- The Rb atoms depolarize much faster due to the high Rb-Xe spin-relaxation cross section. Thus a much higher laser power is needed to polarize Rb;

- The Xe nuclei depolarize before they can diffuse from the pumping to the target chamber because of Xe's slow diffusion. This causes the Xe polarization in the target chamber too small to be useful.

The first problem can be solved by applying laser linewidth narrowing technique and we propose a one-chamber target design which can solve the second problem.

Typical diode lasers used for polarized ^{3}He target are broadband (with $\sigma_\nu \approx 1$ THz). Because the bandwidth of Rb absorption cross section is about 20 GHz for 1 atm gas as determined by pressure broadening, only a fraction of the laser power is absorbed by Rb. The most promising and well tested laser linewidth narrowing technique is to use a diffraction grating to feedback some of the high power laser light back into the diode laser. Using this method a 50 GHz linewidth has been achieved at Univ. of Wisconsin [26, 27] and NIST [28] with a CW output power of 14 W. This technique is also being tested and developed at the medical physics group at UVa. Eight such lasers daisy-chained will provide 120 W of laser power which we will use for the Xe.

Due to the sluggishness of Xe, it is necessary to have $Xe(e, e')$ scattering and Xe-Rb spin exchange happen at the same location, *i.e.* a one-chamber cell. The cell will be composed of only one chamber where optical pumping, spin exchange and electron scattering processes happen at the same place. The chamber will be a 40 cm-long cylinder with a radius of 1 cm. A small dip at the bottom of the cell will collect the liquid Rb so that it is out of the way of the scattered particles.

Figure 6: A possible one-chamber cell design (top view).
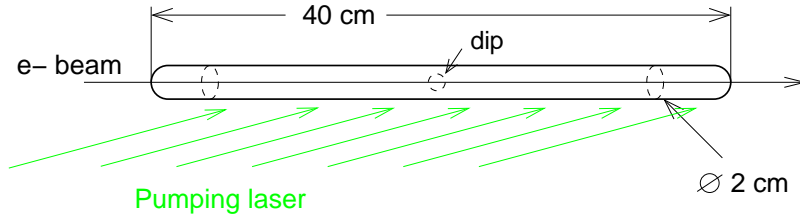
The cell will be heated for Rb to vaporize. To avoid complications and to remove material from the scattered particle paths, we do not plan to use an oven. Hot air will be blown under the cell to vaporize Rb. The laser will provide part of the heating once it is absorbed by the Rb vapor. The current hot air system of the oven can be used with minor modifications. To reduce the material thickness passed by scattered electrons, it might be necessary to use hot ^{4}He gas.

The cell will be heated to 170° and 140°C for the He and Xe cells, respectively. The Rb density is 3×10^{14} (6×10^{13}) cm^{-3} for He(Xe), which is $10^{-(6 \sim 7)}$ of the He(Xe) density and therefore contributions of e-Rb scattering will be negligible.

The laser optics will be setup such that the pumping laser is directed to the right side of the cell at an angle of $\beta = 20.0°$ pointing downstream and slightly to the left. Only one laser direction is necessary for this experiment. The laser polarization can be reversed by inserting half-wave plates in the optics. For one particular laser polarization, the nuclei inside the target are polarized at an angle of $\Theta = \theta - \beta$ and $\phi = 0$ ($\Theta = \beta + \theta$ and $\phi = \pi/2$) for scattered electrons detected by the left (right) HRS (see section 6.2 for definitions of the target spin direction). Combinations of the left and the right HRS data can hence provide information to extract separately $A_\perp$ and $A_\parallel$, or equivalently g_1 and g_2. The laser will be uniformly distributed within an area of 40 cm $\times$ 1 cm=40 cm^2. Some modification of the cell shape might be needed to keep the liquid Rb out of the laser path.

3.2.1 Possible issues with the new design

- The pumping laser will cross the cell glass wall at an angle of $20.0°$. This increase the glass thickness by a factor of 3 compared to pumping at a normal angle to the glass. The power and polarization of the laser might be altered after traversing thick glass. Test will need to be done to estimate what are the effects.

- Some of the laser power will be absorbed by glass, especially when the cell starts to turn brown due to radiation damage. This absorbed power may cause strains that could destroy cell. Tests need to be done to study how much power is absorbed with a brown glass (this can be done e.g. with one of the cell used in former ^{3}He experiments) and how often we need to change cells during the experiment.

- Two-step process: 2 step process (elastic radiative scattering at forward angle on a beam line window followed by elastic scattering of the same electron when it crosses the target wall at sharp angle) is a major source of background for ^{3}He experiments detecting particles at forward angle [39] In our case, the liquid Rb that fills the dip in the bottom of the cell may add significant additional material which increases the probability of interaction after the first step. However, the total angle necessary to re-direct the electrons toward the spectrometer would be larger than the case where the second scattering happen on the side wall. Furthermore, the magnitude of the 2 step process is damped at large energy. All in all, we do not expect significant issue from the 2 step process, although a simulation is needed to quantify the background. [In case of non-negligible background, the shape of the dip can be modified to reduce this background.]

- Beam-photon interactions. The laser light is of similar characteristics as the one used in the Hall A Compton polarimeter (1064 nm with 2kW power for the polarimeter and 795 nm with 120 W of power for the proposed target). The electrons interacting with photons are scattered at very forward angles, $< 1°$, resulting in no contamination of particle detection. The Compton process cross section is rather small so the reduction in the pumping laser power is negligible.

3.3 Figure of merit for polarized target

3.3.1 He and Xe

For a one-chamber cell presented here the target polarization is

$$P_X \;=\; P_{Rb}\frac{\bar{\gamma}_{SE}}{\bar{\gamma}_{SE} + \Gamma} \tag{2}$$

where X denotes He or Xe, γ_{SE} is the spin exchange rate, Γ contains spin destruction rate due to He-He (Xe-Xe), glass wall and beam ionization.

The Rb polarization from Eq. (28) is

$$P_{Rb} = P_\gamma \frac{R_{op}}{R_{op} + [X]\langle \sigma_{SR} v\rangle} \tag{3}$$

where $P_\gamma \approx 100\%$ is the photon polarization, the Rb spin relaxation rate Γ_{SD} is dominated by the Rb-X dipole relaxation and the k_{SE} in Eq. (28) has been rewritten here as $\langle \sigma_{SR} v\rangle$ where σ_{SR} is the X-Rb dipole relaxation cross section and $v = \sqrt{8kT}/(\pi M_{Rb-X})$ is the average thermal speed of X-Rb system; the reduced mass of the Rb-X system is given by $M_{Rb-X} = M_N \frac{A_{Rb} A_X}{A_{Rb} + A_X}$ with A_X the atomic number of Xe or He. The dipole relaxation cross sections between various alkaline and noble gas material can be found in Ref. [31].

The optical pumping power R_{op} is calculated in the paragraph following Eq.(28) and here we express it in terms of the laser power:

$$R_{op} \;=\; 4.5 \times 10^5 f(a) P_{laser}/A_{op}/p \tag{4}$$

where p is the pressure inside the cell, $A_{op} = 40$ is the area of laser spot on the pumping chamber in cm^2 and P_{laser} is in watts. The matching of Rb absorption and the laser spectrum is described by function $f(a) \equiv \int_{-\infty}^{+\infty} e^{-y^2/2}/[1 + (y/a)^2]dy$ where $a \equiv \gamma/(2\sigma_\nu)$, $\gamma \approx p \times 20$ GHz/atm is the pressure broadening of Rb D_1 line and $\sigma_\nu = 50$ GHz is the laser linewidth (FWHM) after utilizing the narrowing technique.

The figure of merit (FOM) for optimizing the statistical error on asymmetries or polarized structure functions is:

$$fom \;\equiv\; P_X^2[X]I_b \propto P_X^2 \mathcal{L} \tag{5}$$

with [X] the Xe or He density and I_b the beam current. Using Eq. (2,4,57), Eq. (5) becomes

$$fom \;=\; [X]I_b\left\{ \left[\frac{R_{op}}{R_{op} + \Gamma_{SR,Rb-X}}\right]\left[\frac{\gamma_{SE}}{\gamma_{SE} + \Gamma_{wall} + \Gamma_{dipole} + \Gamma_{beam}}\right]\right\}^2 \tag{6}$$

where Γ_{wall}, Γ_{dipole} and Γ_{beam} are spin relaxation rate due to collision with wall, He-He (Xe-Xe) collision, and beam ionization effect, respectively.

3.3.2 Ne with hybrid optical pumping technique

Although technique to polarized Xe is mature, it's a very heavy nucleus and there is difficulty in its nuclear corrections, as will be described in the next section. In addition the $(A-1)$ unpolarized nucleons gives a large dilution to the measurement. We study here the possibility to polarized a ligher nucleus, ^{21}Ne, using hybrid optical pumping technique. The advantage of using a Ne target is less dilution and more mature shell model calculations. The disadvantages are less EMC effect (smaller A), less mature polarizing technique (hence more R&D is needed), and the fact that ^{21}Ne spin is $3/2$. Finally the unpaired neutron in ^{21}Ne is not in a s-shell so one expects less effective nucleon polarization. The purpose of this section is to find the best figure of merit for Ne and see if the gain can balance the disadvantages listed above.

For Ne, optical pumping using Rb alone is not fast enough to compensate for Ne's fast spin relaxation due to collision with the cell wall. To overcome this difficulty we can use Rb-K hybrid spin-exchange technique [37]. It has been shown that such technique can improve the spin exchange rate of He by a factor of ten [38]. For Ne, we can use an alkaline alloy made of 3% Rb and 97% of potassium (K) instead of pure Rb. The target cell is heated to $250°$C such that the K density is 10 times higher than the Rb density at $170°$C, and Rb density from the alloy at $250°$C is the same as the Rb vapor density from a pure Rb metal at $170°$. First Rb is polarized via regular optical pumping, then its polarization is transferred to K through spin-exchange. Because the Rb-K spin-exchange rate is very high, $\sim 10^5$ s^{-1}, K atoms can reach the same polarization as Rb. Then Ne nuclei are polarized primarily through spin-exchange with K atoms. This way the optical pumping rate is 10 times higher than a pure-Rb cell with the same pumping laser power. Eq. (6) is also valid for a hybrid cell, except that one need to substitute the spin exchange rate $\gamma_{SE} = \langle \sigma_{SE} v_{Rb-Ne} \rangle [\text{Rb}]$ by $\gamma_{SE} = \langle \sigma_{SE,Rb-Ne} v_{Rb-Ne} \rangle [\text{Rb}] + \langle \sigma_{SE,K-Ne} v_{K-Ne} \rangle [\text{K}]$, and substitute the Rb spin relaxation rate $\Gamma_{SR,Rb-Ne}$ by $\Gamma_{SR,Rb \oplus K} = \Gamma_{SR,Rb} + \mathcal{D} \Gamma_{SR,K}$ with $\mathcal{D} \equiv [\text{K}]/[\text{Rb}]$ and $\Gamma_{SR,K}$ is the spin relaxation rate of K.

If ^{129}Xe turns out to be too difficult for polarized EMC measurement because of its large dilution ($\propto A-1$) and difficulty in nuclear corrections, ^{21}Ne might be a better solution. In that case, a careful study of using ^{21}Ne as a polarized target with hybrid technique and the new cell design should be carried out, including its polarizing efficiency, effects of tensor polarization, and nuclear corrections.

3.3.3 FOM as function of laser power, beam current and fill density

The figure of merit for He, Ne (hybrid) and Xe targets are plotted in Fig. 7. The laser power is 120 W. The beam current used in the one dimensional slice plots are assumed to be 15 μA for He and 30 μA for Ne and Xe. All coefficients used in the calculation are listed in Table 2.

3.3.4 Running conditions determined from FOM

From Fig. 7 we can see that the best running condition for ^{129}Xe is [Xe] $= 1.7$ amg which corresponds to $P_{Xe} \approx 60\%$. Taking into the imperfection of reality we will use $P_{t,Xe} = 50\%$ for Xe at a beam current of 30 μA and a laser power of 120 W. For ^{21}Ne our estimation gives $P_{Ne} \approx 40\%$ and is almost independent of the fill density. However to keep the cell pressure to a manageable level we plan to fill the cell to 5 amg. This provide an FOM sightly higher than Xe.

Table 2: Coefficients used for calculation of the figure of merit. All densities are in amagats and the beam current I_b is in μA. The wall relaxation rate for He is given for a standard-shape GE180 cell, for Ne is for a ϕ1.5 cm spherical Corning 1720 uncoated cell, and for Xe is for a ϕ3 cm spherical Pyrex silicon-coated cell.

Noble gas nucleus	He	Ne	Xe
pumping chamber T_p	170°C	250°C	140°C
$[Rb]$	3×10^{14} cm^{-3}	3×10^{14} cm^{-3}	2×10^{13} cm^{-3}
$[K]$		3×10^{15} cm^{-3}	
R_{op}	see Eq. (4)	see Eq. (4)	see Eq. (4)
Rb-X spin exchange			
σ_{SE} (cm^2) [31]	2.1×10^{-24}	2.9×10^{-24}	1.6×10^{-20}
$\gamma_{SE} = \langle \sigma_{SE} v_{X-Rb} \rangle [Rb]$	$\approx$1/(10-12 hrs)		$\approx$ 1/(20 s)
K-Ne spin exchange			
σ_{SE} (cm^2) [31]		1.5×10^{-24}	
γ_{SE} (Rb+K total)		$\approx$1/(0.7 hrs)	
Rb-X spin relaxation			
$\sigma_{SR,Rb-X}$ (cm^2)		1.8×10^{-23} [31]	1.6×10^{-19} [31]
v_{Rb-X} (cm/s) at T_p	1.7×10^5	8.0×10^4	4.0×10^4
$\langle \sigma_{SR,Rb-X} v \rangle$ (cm^{3}s^{-1})	2×10^{-18} [30]		
$\Gamma_{SR,Rb-X}$ (s^{-1})	54[He]		2.16×10^5[Xe]
K-Ne spin relaxation			
$\sigma_{SR,K-Ne}$ (cm^2)		1.6×10^{-23} [31]	
v_{K-Ne} (cm/s) at T_p		9.0×10^4	
$\Gamma_{SR,Rb \oplus K-Ne}$ (s^{-1})		432[Ne]	
spin relaxation of noble gas			
Γ_{X-X} (dipole)	[He]/744 hrs^{-1}	≈ 0	≈ 0
Γ_{wall}	1/(100-200) hrs^{-1}	1/1 hrs^{-1} [32]	1/1800 s^{-1} [33]
E_{ion} (eV) [34]	24	21	12
$\frac{dE}{dx}$ (MeV g/cm^2) [35]	2.0	1.75	1.25
Γ_{beam} (hrs.$^{-1}$)	$\frac{I_b}{300}$	$\frac{I_b}{30}$	$\frac{I_b}{4}$

Figure 7: Figure of merit $I_b P_t^2 n_X$ for ^{3}He (left), ^{21}Ne (center, hybrid optical-pumping) and ^{129}Xe (right). Shown from top to bottom are: 1) the FOM as a function of beam current I_b (axis pointing to the left) and fill density n_X (axis pointing to the right); 2) the FOM as a function of fill density at the "nominal" beam current (15μA for ^{3}He and 30μA for ^{21}Ne and ^{129}Xe); 3) The target polarization as a function of beam current at a fixed density of [He]=10 amg, [Ne]=5 amg and [Xe]=1 amg; 4) the target polarization as a function of beam current (axis pointing to the left) and fill density (axis pointing to the right); 5) the target polarization as a function of fill density at the "nominal" beam current.
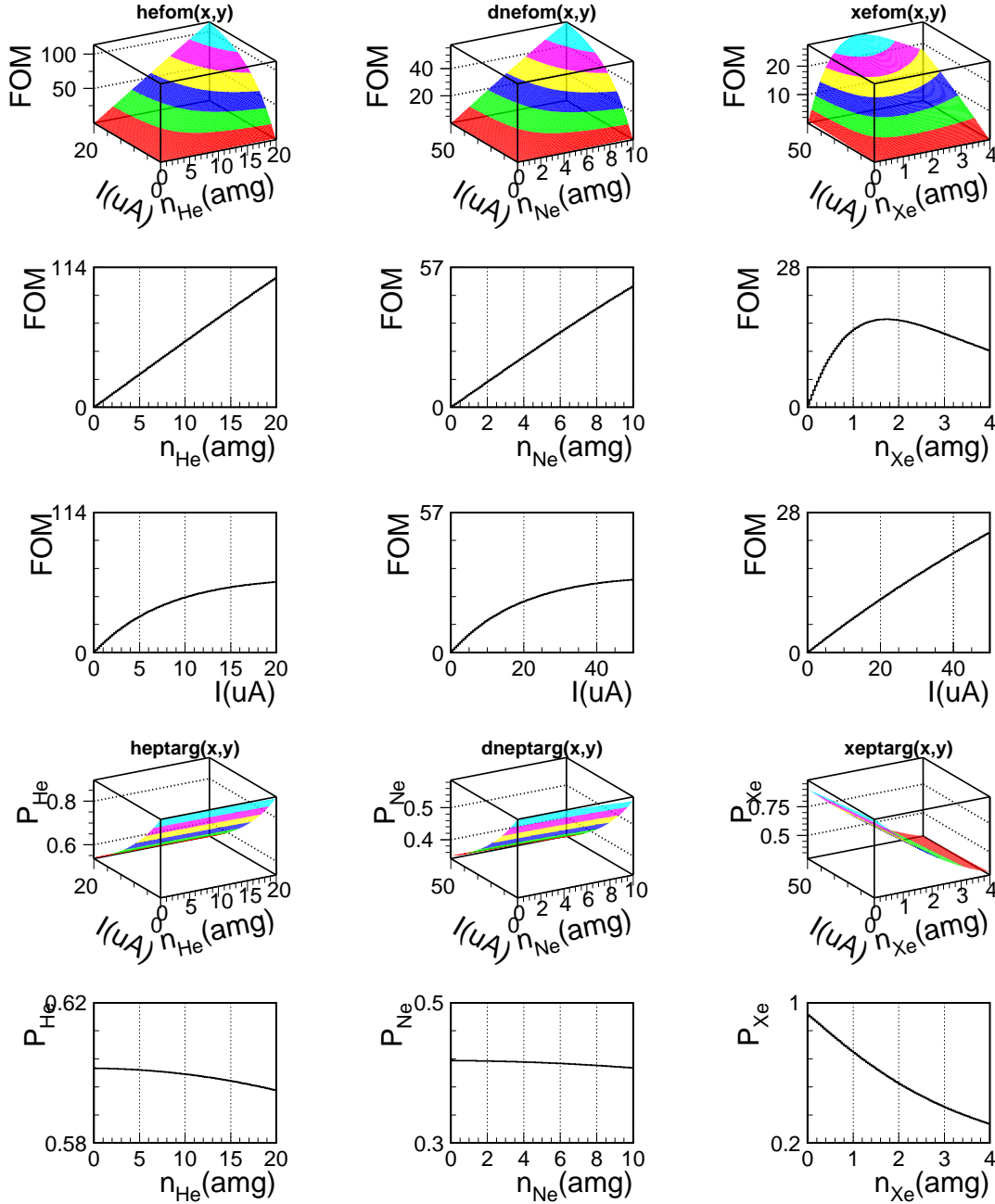
3.3.5 Possible potentials of the new design

Since the pressure of the Xe cell is much lower than what was typically used for ^{3}He cells, it might be possible to use a beam current much higher than 30 μA. Tests need to be done to validate this possibility.

3.4 Target density measurement

The density of polarized target cells were measured by two methods in previous experiments. The first one, called the Archimedes method or the buoyancy method, measures the outer volume of the cell; and the second method is to measure the pressure broadening of the wavelength of D_1 and D_2 light absorbed by rubidium in the cell. The results of both methods were found to be usually in good mutual agreement and the combined results have an uncertainty of $\Delta[\text{He}]/[\text{He}]$ better than 0.9% [36]. The same technique will be used for Xe cells.

3.5 Target polarimetry

The polarization of ^{3}He cells were routinely measured by two polarimeters: NMR and EPR. Here we discuss only the uncertainty of NMR polarimetry: The total systematic uncertainty of a NMR measurement is at 4% level. Of this 4%, about 2.1% is from the water calibration constant, 0.5% from fitting to the NMR signal height, 2.4% from the flux calculations, 0.9% from target density, and 1.0% from other corrections. The uncertainty due to water calibration is independent of the cell used, hence will cancel between ^{3}He and ^{129}Xe measurements. the 2.4% uncertainty in the flux calculations comes from 2% due to mismeasurement of the cell position w.r.t the NMR signal pick-up coils, and 1.3% due to unknown offset [36]. We assume the 1.3% uncertainty due to unknown offset cancels between different cells. Therefore the uncertainty in the EMC ratio is $\sqrt{2}$ times the non-cancelable part, *i.e.* $\sqrt{2} \times 2.46\% = 3.48\%$.

4 Extracting neutron structure function from nuclear data

4.1 From ^{3}He data

The nuclear effects of spin depolarization, binding and Fermi motion are traditionally described within the framework of the convolution approach [40]. In this approximation, nuclear structure functions are in general given by the convolution of the off-shell nucleon structure functions with the light-cone nucleon momentum distributions. Thus, $g_1^{^3{\rm He}}$ can be represented as the convolution of the off-shell neutron $\tilde{g}_1^n$ and the off-shell proton $\tilde{g}_1^p$ spin structure functions with the spin-dependent nucleon light-cone momentum distributions. The motion of the nucleons inside the nucleus (Fermi motion) and their binding are can be readily calculated using the ground-state wave functions of ^{3}He. $g_1^{^3{\rm He}}$ is often approximated by [41]

$$g_1^{^3{\rm He}}(x, Q^2) \;\; = \;\; P_n g_1^n(x, Q^2) + 2P_p g_1^p(x, Q^2) \; . \tag{7}$$

where $P_n(P_p)$ are the effective polarizations of the neutron (proton) inside the polarized ^{3}He nucleus.

In the first approximation to the ground-state wave function of ^{3}He, only the neutron is polarized, which corresponds to the S-wave type interaction between any pair of the nucleons of ^{3}He. In this case, $P_n = 1$ and $P_p = 0$. Realistic approaches to the wave function of ^{3}He include also higher partial waves, notably the D and S' partial waves that arise due to the tensor component of the nucleon-nucleon (N-N) force. This leads to the depolarization of the neutron and the polarization of the protons in ^{3}He. We collect calculations using various models of N-N interactions and 3N forces [41, 42, 43, 44], and take their extreme values as the full uncertainty of $P_{n,p}$, we find:

$$P_n = 0.86^{+0.036}_{-0.02}, \qquad P_p = -0.028^{+0.0094}_{-0.004} \; . \tag{8}$$

A summary of the N-N and 3N forces and the calculations used here can be found in Ref.[45].

4.2 From ^{129}Xe data

The most state-of-art shell model method [46] has been used on the ^{129}Xe, which gives $S_n = 0.362$, $S_p = 0.008$, $L_n = 0.053$, $L_p = 0.077$ [25]. This indicates that ^{129}Xe has effective nucleon polarizations of $P_n = 0.724$ and $P_p = 0.016$. This is the first calculation for heavy nuclei in the region $50 < N, Z < 82$ and it is also indeed the largest shell model calculation ever, with a basis dimension of three billion. The uncertainty of shell model calculation is difficult to determine, however one might be able to measure $P_{n,p}$ of a nucleus from quasi-elastic scattering of a nuclear target, as investigated in the following sections.

4.3 Shell model calculation for ^{21}Ne

Two sets of shell model calculations for ^{21}Ne give $L_p = 0.233$, $L_n = 0.964$, $S_p = 0.011$ and $S_n = 0.292$ [24] and $L_p = 0.23$, $L_n = 0.96$, $S_p = 0.01$ and $S_n = 0.29$ [25], respectively. We note the good agreement between these two calculations. These results give a neutron polarization of $P_n = 0.58$ for ^{21}Ne, lower than both ^{3}He and ^{129}Xe. In addition the nuclear effect in Ne is

expected to be smaller than Xe. At last, the technique to polarize Ne is more difficult than He and Xe. Because of these reasons, in this document we focus only on ^{129}Xe.

4.4 How to test nuclear corrections for Xe?

The nucleon polarizations we use in the nuclear correction for Xe should be tested from an independent measurement. We do not know exactly yet how to do such test, perhaps from quasi-elastic measurements designed specifically for ^{129}Xe, in a fashion similar to the approved experiment on testing the nuclear correction for ^{3}He [47]. Support from both experimentalists and theorists will be crucial for securing the nuclear corrections for heavy nuclei.

5 Systematic Uncertainties

5.1 Experimental Systematics

In this section we discuss systematic uncertainties on the polarized cross sections. The dominant uncertainties, including both target correlated and un-correlated, are:

- HRS acceptance: 2%;

- Rad. corrections, assume 2%;

- Target thickness (density): 1%;

- Beam polarization: 1% from the green Compton or 3% from either Moller or IR Compton;

- Target polarization: 4% in either $P_{t,He}$ or $P_{t,Xe}$;

- Beam current: 1%

- Nuclear corrections: 3.2% full uncertainty for ^{3}He. We assume a 4% uncertainty for $P_{n,Xe}/P_{n,He}$.

Other uncertainties include:

- false asymmetry and other helicity-correlated asymmetries: This can be controlled by the luminosity monitor to 10 ppb and is negligible.

- DAQ deadtime correction: the uncertainty on the deadtime correction is 0.3% as described in Section 2.3, and is negligible.

- pair production background:

- pion background.

When forming the EMC ratio $R = g_1^{He}/g_1^{Xe}$, the Xe-He target correlated systematics cancel out:

- HRS acceptance uncertainty cancels;

- Radiative correction uncertainty mostly cancels and the net effect on the EMC ratio is negligible. This part is explained in Appendix B.

- Target density partly cancels because the same (pressure broadening) method will be used for both target. We assume the error is divided by factor of 2;

- Beam current: error comes from BCM calibrations and cancel;

- Beam polarization uncertainty cancels because the same polarimetry will be used and the target-uncorrelated part is only the statistical uncertainty, which is negligible;

- Target polarization: 3.5% in the ratio $P_{t,He}/P_{t,Xe}$ as discussed in section 3.5.

The target un-correlated systematic uncertainty for either g_1^{He} or g_1^{Xe} is therefore 0.5% from target thickness (density), and negligible amount from radiative corrections, false and helicity-correlated beam asymmetries.. Taking the ratio g_1^{He}/g_1^{Xe} will scale this uncertainty by $\sqrt{2}$, giving an uncertainty of 0.7%. Adding the uncertainty from target polarization, we obtain an experimental systematic uncertainty on the EMC ratio of 3.6%.

5.2 Uncertainties due to nuclear corrections

The uncertainty on the EMC ratio due to P_n in the nuclear correction is assumed to be 4%. In addition to P_n, the polarization of the proton inside nuclear target also contribute to the polarized cross sections. The uncertainty on g_{1n} due to proton polarization can be estimated by

$$\Delta g_{1n,\mathrm{mod}} = \frac{\tilde{P}_p}{\tilde{P}_n} \frac{g_{1p}}{g_{1n}} \tag{9}$$

The P_p for He has a full uncertainty of $(-0.004, 0.0094)$ and is expected to be improved by at least a factor of 2 after the completion of E05-102 [47]. We assume a 30% uncertainty on P_p for the Xe and found a uncertainty of 2.50% for g_{1n}^{He} and 1.33% for g_{1n}^{Xe}. These add a 2.83% uncertainty to the ratio $g_{1n}^{\mathrm{Xe}}/g_{1n}^{\mathrm{He}}$.

5.3 Parity-Violation Backgrounds

The parity violation asymmetry is of the order of 100 ppm at $Q^2 = 1$ (GeV/c)^2, comparable to the spin asymmetry of Xe. We plan to flip the target polarization for half of the statistics by reversing the polarization of pumping lasers. The polarized cross section extracted from one target polarization by taking the difference between + and - beam helicity is then averaged with that from the opposite target polarization by taking the difference between - and + beam helicity (note the reversal in beam helicity), this way the parity-violating components cancel.

5.4 Other Backgrounds

There are background events from pion and pair production processes. In addition, events from target cell glass windows and the unpolarized N_2 gas in the target cell will dilute the measurement. All these should be studied carefully once a full proposal is being developed. However from experience of previous polarized ^{3}He experiments, we do not expect any issue from these background.

6 Data Analysis Procedure and Kinematics Optimization

6.1 Extracting Polarized Cross Section from Raw Data

A cross section can be expressed as

$$\sigma = \frac{N}{\eta_{LT} t} \frac{1}{\mathcal{L} \Delta\Omega \Delta E'} \tag{10}$$

where N is number of events collected within a time of t, η_{LT} is the DAQ livetime, $\mathcal{L} = I d_t \rho_t$ is the luminosity with I the beam current, d_t the target length and ρ_t the target density. $\Delta\Omega$ and $\Delta E'$ are the spectrometer angular and momentum acceptances, respectively. The statistical uncertainty of cross section is

$$\Delta\sigma = \frac{\sqrt{N}}{\eta_{LT} t} \frac{1}{\mathcal{L} \Delta\Omega \Delta E'} \tag{11}$$

Defining the rate as $R = N/t$ we can write

$$\Delta\sigma = \sqrt{\frac{R}{t}} \frac{1}{\eta_{LT} \mathcal{L} \Delta\Omega \Delta E'} \tag{12}$$

For a given target spin orientation we measure the difference in cross section between opposite beam helicity states:

$$\sigma_{diff} = \sigma^+ - \sigma^- = \left(\frac{N^+}{\eta_{LT}^+ \mathcal{L}^+ t^+} - \frac{N^-}{\eta_{LT}^- \mathcal{L}^- t^-} \right) \frac{1}{\Delta\Omega \Delta E'} \tag{13}$$

where $N^+ = \frac{N}{2}(1 + A) + N_u/2$ and $N^- = \frac{N}{2}(1 - A) + N_u/2$ with $N^{+(-)}$ the event counts from the polarized material in the target for a +(-) beam helicity and N_u the event counts from unpolarized material. For the purpose of rate and statistical uncertainty estimation we neglect the asymmetry in beam current and timing of helicity pulses, *i.e.* $\mathcal{L}^+ = \mathcal{L}^-$ and $t^+ = t^- = t/2$. We also assume that there is no event loss, $\eta_{LT} = 100\%$, and rewrite σ_{diff} as

$$\sigma_{diff} = \frac{N^+ - N^-}{t/2} \frac{1}{\mathcal{L} \Delta\Omega \Delta E'} \tag{14}$$

The uncertainty is:

$$\Delta\sigma_{diff} = \frac{2\sqrt{(\Delta N^+)^2 + (\Delta N^-)^2}}{t \mathcal{L} \Delta\Omega \Delta E'} = \frac{2\sqrt{\frac{N}{2}(1 + A) + \frac{N}{2}(1 - A) + N_u}}{t \mathcal{L} \Delta\Omega \Delta E'}$$

$$= \frac{2\sqrt{N + N_u}}{t \mathcal{L} \Delta\Omega \Delta E'} = \sqrt{\frac{R_{tot}}{t}} \frac{2}{\mathcal{L} \Delta\Omega \Delta E'} \tag{15}$$

where R_{tot} is the sum of polarized and unpolarized rates. Correcting σ_{diff} by the target and beam polarizations P_t and P_b, and the effective nucleon polarization P_n, we obtain

$$\sigma_{\vec{S}} = \frac{\sigma_{diff}}{P_b P_t P_n} \tag{16}$$

$$\text{and } \Delta\sigma_{\vec{S}} = \sqrt{\frac{R_{tot}}{t}} \frac{2}{\mathcal{L} \Delta\Omega \Delta E'} \frac{1}{P_b P_t P_n} \tag{17}$$

where $\vec{S}$ denotes the target spin direction.

6.2 Extracting $g_{1,2}$ from Polarized Cross Sections

The cross section differences for a particular target spin direction $\vec{S}$ is

$$\frac{d^2\sigma_{\downarrow,\vec{S}} - d^2\sigma_{\uparrow,\vec{S}}}{d\Omega dE'} = \frac{4\alpha^2 E'}{MEQ^2}\left\{\frac{E\cos\beta + E'\cos\Theta}{\nu}g_1 + \frac{2EE'}{\nu^2}(\cos\Theta - \cos\beta)g_2\right\} \quad (18)$$

where angle β (Θ) is formed by $\vec{S}$ and the incident (outgoing) electron's momentum $\vec{k}$ ($\vec{k}'$), and ϕ is the angle formed by plane $(\vec{k},\vec{S})$ and the scattering plane $(\vec{k},\vec{k}')$, as shown in Fig. 8. They satisfy $\cos\Theta = \sin\theta\sin\beta\cos\phi + \cos\theta\cos\beta$. For our target design, the polarized cross sections

Figure 8: Definition of target spin orientation.
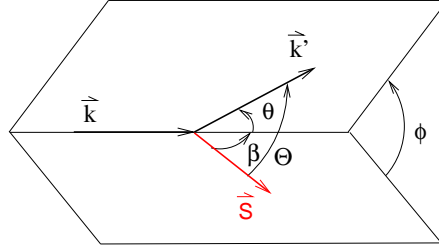
measured on the left and the right HRS are

$$\sigma_L = a(bg_1 + cg_2), \qquad \sigma_R = a(dg_1 + eg_2) \quad (19)$$

where the kinematic coefficients defined as follows:

$$a = \frac{4\alpha^2 E'}{MQ^2 E}$$

$$b = \frac{\left[E\cos\beta + E'\cos(\beta - \theta)\right]}{\nu}, \; c = \frac{2EE'}{\nu}\left[\cos(\beta - \theta) - \cos\beta\right],$$

$$d = \frac{\left[E\cos\beta + E'\cos(\beta + \theta)\right]}{\nu} \text{ and } e = \frac{2EE'}{\nu}\left[\cos(\beta + \theta) - \cos\beta\right].$$

g_1 and g_2 can be extracted as

$$g_1 = f(e\sigma_L - c\sigma_R), \qquad g_2 = f(-d\sigma_L + b\sigma_R) \quad (20)$$

where $f = 1/[a(be - cd)]$. The statistical error on g_1 and g_2 are:

$$\Delta g_1 = f\sqrt{e^2 + c^2}\Delta\sigma_{L,R} = f\sqrt{e^2 + c^2}\sqrt{\frac{R_{tot}}{t}}\frac{2}{\mathcal{L}\Delta\Omega\Delta E'}\frac{1}{P_b P_t P_n} \quad (21)$$

$$\Delta g_2 = f\sqrt{d^2 + b^2}\Delta\sigma_{L,R} = f\sqrt{d^2 + b^2}\sqrt{\frac{R_{tot}}{t}}\frac{2}{\mathcal{L}\Delta\Omega\Delta E'}\frac{1}{P_b P_t P_n} \quad (22)$$

where R_{tot} is the rate on either left or right HRS.

The time allocation between He and Xe in order to optimize the uncertainty on the ratio of g_{1n}^A/g_{1n} is:

$$\frac{T_{\mathrm{He}}}{T_{\mathrm{Xe}}} = \frac{P_{t,\mathrm{Xe}}P_{n,\mathrm{Xe}}}{P_{t,\mathrm{He}}P_{n,\mathrm{He}}}\sqrt{\frac{\sigma_{\mathrm{He}}}{\sigma_{\mathrm{Xe}}}\frac{I_{\mathrm{Xe}}[\mathrm{Xe}]}{I_{\mathrm{He}}[\mathrm{He}]}} \tag{23}$$

For the kinematics we consider (see next section) we obtain $\frac{T_{\mathrm{He}}}{T_{\mathrm{Xe}}} = 0.14$.

6.3   Size of Measured Asymmetries

We estimate the size of measured asymmetries in order to determine to what level we need to control the helicity-correlated specifications of the beam. The asymmetry for a particular target spin direction is

$$\begin{aligned} A_{\vec{S}} = {} & \frac{1-\epsilon}{F_1(x,Q^2)(1+\epsilon R)} \\ & \times \left[\frac{(E\cos\beta + E'\cos\Theta)}{\nu}g_1(x,Q^2) + \frac{2EE'}{\nu^2}(\cos\Theta - \cos\beta)g_2(x,Q^2)\right] \end{aligned} \tag{24}$$

where ϵ is the magnitude of the virtual photon's transverse polarization:

$$\epsilon = \frac{1}{1 + 2(1+\gamma^2)\tan^2(\theta/2)} \tag{25}$$

with $\gamma^2 = Q^2/\nu^2$ and $R \equiv \sigma_L/\sigma_T$. Comparing to the asymmetries for parallel and perpendicular target spin settings

$$A_{\parallel} = \frac{1-\epsilon}{1+\epsilon R}\frac{\left[(E + E'\cos\theta)g_1(x,Q^2) - 2Mxg_2(x,Q^2)\right]}{\nu F_1(x,Q^2)} \tag{26}$$

$$A_{\perp} = \frac{(1-\epsilon)\sin\theta}{1+\epsilon R}\frac{\left[g_1(x,Q^2) + \frac{2E}{\nu}g_2(x,Q^2)\right]}{\nu F_1(x,Q^2)} \tag{27}$$

we find for our target spin configuration $A_L = A_{\parallel}\cos\beta + A_{\perp}\sin\beta$ and $A_R = A_{\parallel}\cos\beta - A_{\perp}\sin\beta$. The measured asymmetries on the left (right) HRS are -0.604% (-0.623%) for He and $-144.16(-148.54)$ ppm for Xe. We would like to have helicity-correlated beam asymmetry and false asymmetries to be well below 1% of the measured asymmetry, hence we require both to be controlled below 1 ppm.

6.4   Kinematics Optimization and Rate Estimation

We use the NMC95 fit [49] to calculate the e^- rate, and calculate the best precision we can achieve for g_1 within a certain amount of time. Pion and positron (pair production) rates are estimated using Wiser's [48] fit with both results multiplied by 2 for a more conservative estimation for these backgrounds. The optimized kinematics are given in Table 3. Expected values for g_{1n} and g_{1n}^A are calculated using the method described in section 1.3. The Wandzura-Wilczek relation [15] was used to estimate the size of g_{2n} and g_{2n}^A since results from a recent Hall A experiment E97-103 on g_{2n} did not find large deviation from this leading-twist component at $Q^2 > 1$ (GeV/$c)^2$ [50].

Table 3: Kinematics for the proposed measurement. Rates and running times are for one HRS. For the FOM, we use $P_{Xe} = 50\%$, $[Xe] = 1.7$ amg and $I_b = 30\mu$A as described in section 3.3. The total production time is 20.0 days using two HRSs.

| Kinematics	
x_{Bj}	0.19
Q^2 (GeV/c)^2	1.03
E (GeV)	6.0
E' (GeV)	3.10
θ	13.5°
W (GeV)	2.30
Cross sections and rates	
$d\sigma^n/d\Omega dE'$ (μb/GeV/sr)	0.10
$d\sigma^{He}/d\Omega dE'$ (μb/GeV/sr)	0.28
$d\sigma^{Xe}/d\Omega dE'$ (μb/GeV/sr)	11.49
He rate (Hz)	0.28
Xe rate (KHz)	11.49
Backgrounds	
π^-/e^- ratio	74.5%
e^+/e^- ratio	0.150%
Running times	
He (hrs.)	83.9
Xe (hrs.)	876.1
Structure functions	
g_{1n}	−0.0878
g_{1n}^A(val) [9]	−0.0917
g_{1n}^A [10]	−0.1032
g_{1n}^A/g_{1n} (val) [9]	1.0444
g_{1n}^A/g_{1n}[10]	1.1747
g_{2n}	0.0558
g_{2n}^A(val) [9]	0.0605
g_{2n}^A [10]	0.0702
Expected Measured Asymmetries (L, R)	
A_{meas}^{He}	−0.604%, −0.623%
A_{meas}^{Xe} (ppm)	−144.16, −148.54
Expected Statistical Uncertainties	
Δg_1^{He} (stat.)	0.0015
Δg_1^{Xe} (stat.)	0.0047
Δg_2^{He} (stat.)	0.0114
Δg_2^{Xe} (stat.)	0.0370
$\Delta(g_{1n}^A/g_{1n})$(stat.)	0.0566

7 Beam Time Request and Expected Results

7.1 Expected results on polarized EMC ratio for the neutron

The expected results are shown in table 4 and Fig. 9.

Table 4: Expected results on g_{1n}, g_{1n}^A and their ratio from the proposed measurements. The systematic uncertainties include only the point-to-point (target-uncorrelated) uncertainties of experimental systematics and nuclear corrections.

x_{Bj}	0.19
$\Delta(g_{1n})$	± 0.0015(stat.)$\pm 3.55\%$(syst.)
$\Delta(g_{1n}^A)$	± 0.0047(stat.)$\pm 4.52\%$(syst.)
$\Delta(g_{1n}^A/g_{1n})$	± 0.0566 (stat.)$\pm 3.57\%$ (exp.) $\pm 4.0\%$ (P_n) $\pm 2.83\%$ (P_p)

Figure 9: Expected results on g_{1n} (left) from ^{3}He (solid circle) and ^{129}Xe (solid square) and their ratio (right) from the proposed measurement. The inner ticks at each point (invisible for ^{3}He) show the statistical uncertainty and the outer ones show the quadrature of statistical and point-to-point (target-uncorrelated) systematic uncertainties. For clarity, previous world data on g_{1n} are plotted in light (cyan) color (they were measured at different Q^2 than our proposed kinematics and are not evolved here). The three curves shown in the left plot are: free nucleon value on structure functions (blue) based on world parametrization of polarized PDFs; and the in-medium values calculated from Ref. [9] (red) and Ref. [10] (green). The two curves shown in right plot are the EMC ratios calculated from Ref. [9] (red) and Ref. [10] (green).
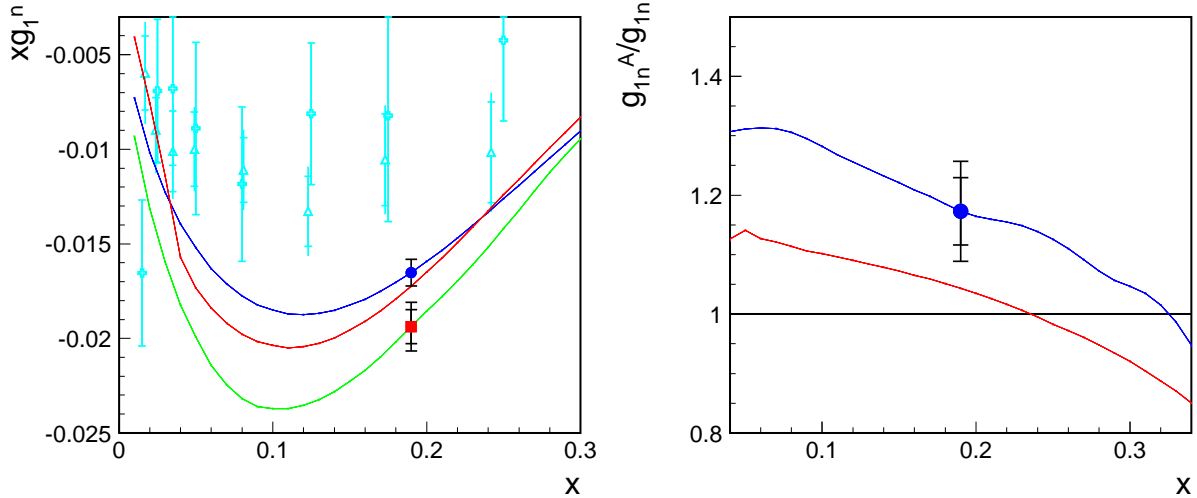
7.2 Beam Time Request

We request 24 PAC days of beam time for the proposed pioneering measurements. Among these 24 days, production takes 20.2 days including 20.0 days for polarized target runs and 4 hours for reference cell runs; we need two days for commissioning, 8 hours for changing target from ^{3}He to ^{129}Xe, 8 hours for other configuration change and 8 hours for beam pass change and Moller measurements. Setup of the Compton polarimeter can be done during commissioning. Compton polarimetry is parasitic and do not require separate beam time.

7.3 Discussions on Ne

In section 3.3.4 we have shown that a polarized Ne target can in principle provide a similar or slightly higher figure of merit $I_b P_t^2 \rho$ as polarized Xe, here ρ is the target density. To study how well g_{1n} can be measured, one needs to include also nucleon effective polarizations and the $1/A$ dilution, *i.e.* times the target FOM by P_n^2/A. Taking $P_n^{Xe} = 0.72$ and $P_n^{Ne} = 0.58$, we obtain that the FOM of Ne target is $(P_n^{Ne}/P_n^{Xe})^2 (A_{Xe}/A_{Ne}) \approx 4$ times better than Xe. This means ^{21}Ne may provide a similar statistical precision as Xe on g_{1n}^A within half amount of beamtime. However, one expect the EMC effect ($\propto A^{-1/3}$) on Ne to be smaller than Xe and more R&D effort is required on the new target design to integrate the hybrid optical pumping technique for the Ne.

8 Summary

We studied the feasibility to measure the medium modification of polarized neutron structure function g_{1n}. The polarized EMC ratio $R_1^{emc} \equiv g_{1n}^A/g_{1n}$ can be measured at $x = 0.19$ to a precision of $\Delta R_1^{emc} = 0.0807$. The size of polarized EMC ratio is unknown so far, calculation from a chiral quark soliton model predicts $R_1^{emc} = 1.1747$ at the proposed kinematics and that from the NJL model gives $R_1^{emc} = 1.0444$. Results from such experiment will therefore be pioneering in the field of medium modification of the nucleon structure and might be helpful in distinguishing between models.

The proposed measurement is challenging in both theoretical and experimental aspects. It will require development of a polarized ^{129}Xe target. Although all required technique to polarized ^{129}Xe already existed, such development may take a couple of years. Theoretically, how to do nuclear corrections for ^{129}Xe remains a challenge for nuclear theorists. It is preferred to perform an independent measurement just to test its nuclear corrections. If nuclear corrections for ^{129}Xe turns out to be too difficult, ^{21}Ne might be a more suitable target, in which case careful studies need to be carried out on its polarizing technique and again nuclear corrections. If strong support can be provided by the Program Advisory Committee and the JLab management, we will start development on the polarized target and calculations and supporting meausurements for the nuclear corrections.

A Target Polarization of a Standard Two-Chamber Cell

A.1 Standard Two-Chamber Cell Design Used Previously

During previous polarized ^{3}He experiments we have been using a standard two-chamber cell design, as shown in Fig. 10, with some definitions used to describe the cell geometry.

Figure 10: A standard two-chamber target cell. The cell consists a spherical "pumping chamber" and a cylindrical "target chamber", and a "transfer tube" connecting the two chambers. The electron beam pass through the target chamber as shown in the side view.
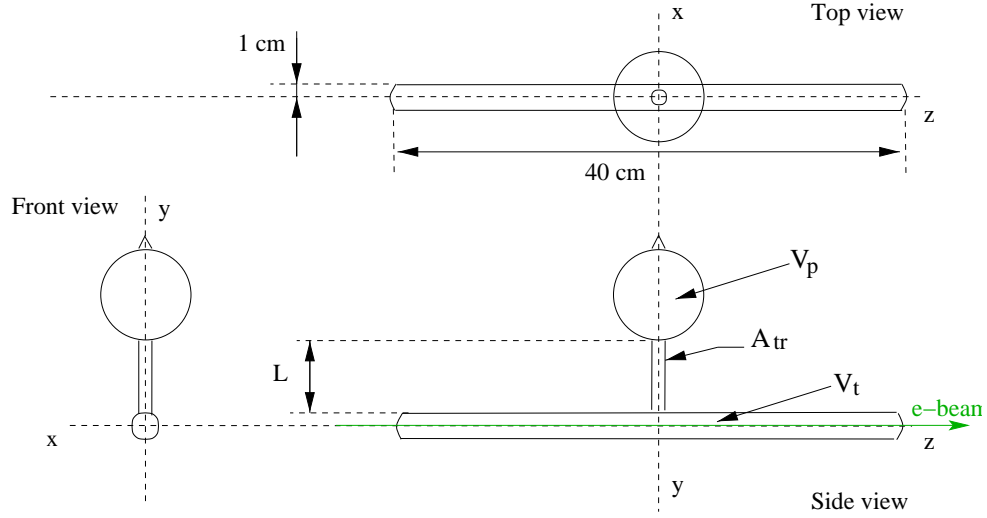
A.2 Optical Pumping of Rb

Using optical pumping the polarization of Rb at equilibrium can be calculated as

$$\langle P_{Rb} \rangle = \frac{R_{op}}{R_{op} + \Gamma_{SD}} \tag{28}$$

where the optical pumping power is in principle given by

$$R_{op} = \int \Phi(\nu)\sigma(\nu)d\nu \tag{29}$$

with $\Phi(\nu)d\nu$ the photon flux and $\sigma(\nu)$ the light-absorption cross section. The total absorption cross section is approximately

$$\sigma_{tot} \equiv \int_{-\infty}^{+\infty} \sigma(\nu)d\nu = \pi r_e c f \tag{30}$$

with $r_e = 2.82 \times 10^{-13}$ cm the classic radius of electrons, $f = 1/3$ the oscillator strength of Rb's D_1 line and c the speed of light. The cross section should follow a Lorenzian distribution.

$$\sigma(\nu) = \sigma_{tot} \frac{1}{(\pi\gamma/2)\left[\left(\frac{\nu-\nu_0}{\gamma/2}\right)^2 + 1\right]} \tag{31}$$

where γ is the pressure broadening of D_1 line, measured to be $\gamma = [He]18.7 \pm 0.2$ GHz/amg (FWHM) for ^{3}He. The value at the absorption peak is

$$\sigma(\nu_0) = \frac{2}{\pi\gamma} \int_{-\infty}^{+\infty} \sigma(\nu)d\nu \tag{32}$$

The laser power is a Gaussian distribution with a center tuned to 795 nm and a FWHM of σ_λ=2 nm. This gives

$$\int_{-\infty}^{+\infty} \Phi(\nu)d\nu = \frac{P_{laser}}{\pi r^2 h\nu_0} \text{ and } \Phi(\nu) = \frac{P_{laser}}{\pi r^2 h\nu_0}\frac{1}{\sqrt{2\pi}\sigma_\nu}e^{-\frac{(\nu-\nu_0)^2}{2\sigma_\nu^2}} \tag{33}$$

where r is the radius of laser spot at the pumping chamber and P_{laser} is the total laser power. For a ^{3}He target we have $r = 3$ cm and $\int_{-\infty}^{+\infty} \Phi(\nu)d\nu \approx 10^{19}$ photons/cm^2/s. The photon flux at the peak of the spectrum is

$$\Phi(\nu_0) = \frac{1}{\sqrt{2\pi}\sigma_\nu} \int_{-\infty}^{+\infty} \Phi(\nu)d\nu \tag{34}$$

where $\sigma_\nu = \frac{c}{\lambda}\frac{\sigma_\lambda}{\lambda} \approx 10^3$ GHz and thus $\Phi(\nu_0) \approx 5 \times 10^6$ photons/cm^2.

The pumpint power is then

$$R_{op} = \sqrt{\frac{2}{\pi}}\frac{\sigma_{tot}}{\pi\gamma}\frac{P_{laser}}{\pi r^2 h\nu_0} \int_{-\infty}^{+\infty} e^{-y^2/2}\frac{1}{1+(y/a)^2}dy \tag{35}$$

with $a \equiv \gamma/(2\sigma_\nu)$. The integral on the r.h.s. increases monotonically as a increases and starts to flatten out above $a \approx (2-3)$. From Eq. (35) one can see that for a fixed fill pressure the optical pumping power is the highest when the laser linewidth is about the same size as the pressure broadening of the Rb.

For typical ^{3}He target used at JLab, [He]=10 amg [3] and $\sigma(\nu_0) \approx 3 \times 10^{-14}$ cm^2. Since the diode lasers used have a linewidth of $\sigma_\nu \approx 10^{12}$ Hz $\gg \gamma = 1.87 \times 10^{11}$ Hz, only a fraction of the laser power is absorbed and one has

$$R_{op} \approx \Phi(\nu_0)\sigma_{tot} = \frac{P_{laser}/(\pi r^2 h\nu_0)}{\sqrt{2\pi}\sigma_\nu}\pi r_e cf$$

and for typical ^{3}He target is 4.4×10^4 s^{-1} for a laser power of $P_{laser} = 100$ W.

For ^{129}Xe the pressure broadening is measured to be similar to ^{3}He [30]. However, since Rb polarization relaxes much faster when it spin-exchanges with Xe than He, laser narrowing technique is required to achieve a reasonable Rb (and hence Xe) polarization.

---

[3] 1 amagat = 2.70×10^{19} cm^{-3}

Γ_{SD} is the spin destruction rate of Rb atoms and can be calculated as

$$\Gamma_{SD} = k_{Rb-X}[X] + k_{Rb-N_2}[N_2] + k_{Rb-Rb}[Rb] \tag{36}$$

where X is the nucleus being polarized and $[X]$, $[N_2]$ and $[Rb]$ are the number density of X, N_2 and Rb, respectively. Within a factor of two we have $k_{Rb-Rb} = 8 \times 10^{-13}$, $k_{Rb-^3He} \leq 2 \times 10^{-18}$, $k_{Rb-N_2} = 8 \times 10^{-18}$ [30] and $k_{Rb-^{129}Xe} = 3.7 \times 10^{-16}$ cm^3/s [53]. The ^{3}He or ^{129}Xe and the N_2 densities are determined by the filled density and the operating temperature. The Rb density can be calculated by the Killian formula [54]:

$$\log(p(T)) = 10.55 - \frac{4132}{T} \tag{37}$$

where $p(T)$ is the Rb vapor pressure in bars in the CGS unit (1 CGS bar = 10^6 dyne/cm^2 = 10^6 g-cm^2/s = 0.1 Pascal), and T is the temperature in Kelvin. Using $p = nkT$ and the Boltzmann constant $k = 1.38 \times 10^{-23}$ J/K, we obtain

$$[Rb] = \frac{10^{10.55 - 4132/T}}{1.38 \times 10^{-16}T} \text{ cm}^{-3} \tag{38}$$

which gives $[Rb] = 3 \times 10^{14}$ cm^{-3} for $T_p = 170^\circ$C and 2×10^{13} cm^{-3} for $T_p = 120^\circ$C.

The destruction rate for a typical ^{3}He target is rather small compared to optical pumping power. For a pumping chamber filled by 8 amg ^{3}He and Rb at a temperature of 170°C, one has $[^3He] = 2.16 \times 10^{20}$, $[N_2] = 1.8 \times 10^{18}$ and $[Rb] = 4 \times 10^{14}$ cm^{-3}, giving $\Gamma_{SD}^{He} = 432$ (Rb-^{3}He)+14 (Rb-N$_2$)+320 (Rb-Rb) = 766 s^{-1}. Rb maximum polarization is therefore $\langle P_{Rb} \rangle^{He} = \frac{44000}{44000+766} \approx 98\%$. The destruction rate for a Xe target is much larger because of the large dipole cross section between Rb and Xe, which results in a smaller Rb polarization. Assuming a 120°C pumping chamber temperature and a pumping chamber density of 8 amg for Xe, we have $[^{129}Xe] = 2.16 \times 10^{20}$, $[Rb] = 2 \times 10^{13}$ cm^{-3} and $\Gamma_{SD}^{Xe} = 79920$ (Rb-^{129}Xe)+14 (Rb-N$_2$)+16 (Rb-Rb) = 79950 s^{-1}. Rb maximum polarization is thus $\langle P_{Rb} \rangle^{Xe} = \frac{44000}{44000+79950} \approx 35\%$.

A.3 Spin Exchange between Rb and Nobel Gas Nuclei

The polarization is then transferred from Rb atoms to nuclei. The nuclear polarization evolves with time as:

$$P_X(t) = \langle P_{Rb} \rangle \frac{\gamma_{\bar{S}E}}{\gamma_{\bar{S}E} + \Gamma} \left\{ 1 - e^{[-(\gamma_{SE}+\Gamma)t]} \right\} \tag{39}$$

where $\gamma_{SE} = k_{SE}[Rb]$ and k_{SE} is the spin exchange coefficient. $\gamma_{\bar{S}E}$ is the effective coefficient which differs from γ_{SE} for a two-chamber cell or if the laser spot does not cover the full pumping chamber: $\gamma_{\bar{S}E} = \frac{n_p V_p}{n_p V_p + n_t V_t} \times \frac{V_{p,covered}}{V_p} \times \gamma_{SE}$, where $V_{p,covered}$ is the volume covered by laser, $n_{p(t)}$ and $V_{p(t)}$ are the density and volume of the pumping (target) chambers, respectively. The densities are given by

$$n_t = n_0 \left[1 + \frac{V_p}{V_{tot}} \left(\frac{T_t}{T_p} - 1 \right) \right]^{-1} \tag{40}$$

$$n_p = n_0 \left[1 + \frac{V_t}{V_{tot}} \left(\frac{T_p}{T_t} - 1 \right) \right]^{-1} \tag{41}$$

32

where $T_{p(t)}$ is the pumping (target) chamber temperature. The spin exchange rate for ^{3}He for a Rb density at 170°C is $\gamma_{SE}^{He} = 4.8 \times 10^{-5}$ s^{-1}=1/(5.8 hrs.). For ^{129}Xe one has [53]

$$\gamma_{SE}^{Xe} = k_{SE}^{Xe}[\text{Rb}] \text{ and} \tag{42}$$

$$\gamma_{SE}^{Xe} = \frac{\gamma_M \zeta}{2.48 \times 10^{19} \text{ cm}^{-3}} \frac{1}{P_a} + \langle \sigma \nu \rangle \tag{43}$$

where $\zeta = 0.1791$. The first and the second terms corresponds to Rb-Xe van der Waals molecular and binary spin-exchange contributions, respectively. The Xe pressure determines the quantity P_a as:

$$\frac{1}{P_a} = \frac{760 \text{ Torr}}{P_{Xe}} \left(\frac{1}{1 + br} \right) \tag{44}$$

with $b = 0.275$ and $r = P_{N_2}/P_{Xe}$. γ_M and $\langle \sigma \nu \rangle$ have been measured to be $\gamma_M = (2.92 \pm 0.18 \pm 0.41) \times 10^4$ s^{-1} and $\langle \sigma \nu \rangle = (3.70 \pm 0.15 \pm 0.55) \times 10^{-16}$ cm^{3}s^{-1}. For $[\text{Rb}] = 2 \times 10^{13}$ cm^{-3} (120°C), one has $k_{SE}^{Xe} \approx (21.09 + 3.7) \times 10^{-16}$ cm^{3}s^{-1} and $\gamma_{SE}^{Xe} \approx 5 \times 10^{-2}$ s^{-1}=1/(20 s).

Γ is the polarization destruction rate of the nuclei and can be expressed as

$$\Gamma = \Gamma_{Dipole} + \Gamma_{wall} + \Gamma_{\nabla B} + \Gamma_{Beam} \tag{45}$$

For ^{3}He we have the relaxation rate due to dipole interactions between the He-He molecule's spins and rotational angular momentum $\Gamma_{Dipole} = \frac{[^3\text{He}]}{744}$ hrs^{-1} with $[^3\text{He}]$ in amagats. The Xe-Xe dipole relaxation time is smaller than He-He and does not contribute noticeably to ^{129}Xe spin destruction [51]. For Xe one also has nuclear spin rotation given by $T_{NSR}[\text{Xe}] = 2 \times 10^5$ s-amg, which is negligible within the Xe density of our interest. $\Gamma_{\nabla B}$ is usually negligible when the field gradients are at the order of a few mGauss/cm. Note that the polarization destruction rate is different in the pumping and the target chamber of a two-chamber target because of the different temperature and thus the different densities [X].

The beam depolarization has been estimated as $\Gamma_{Beam} = (n_a + n_m)\Gamma_I$ where n_a is the number of ^{3}He atoms depolarized over number ionized and n_m is the number of ^{3}He$_2$ molecules over number ionized. Because of the presence of N$_2$, n_m is usually negligible. This equation also applies to Xe. The beam depolarization coefficient Γ_I for nuclear matter can be estimated by [52]

$$\Gamma_I = I_b \left(\frac{dE}{dx} \right)_X \frac{M_X L}{E_{ion,X} V} \tag{46}$$

where I_b is beam current in number of e^- per second, $\frac{dE}{dx}$ is the minimal ionization energy loss in MeV/g/cm^2 when electrons pass through matter, $E_{ion,X}$ is the mean energy to produce an ion pair from a target atom, L and V are length and volume of the target cell scattering chambers, respectively. The ionization energies are $E_{ion,^3\text{He}} = 32$ eV [55] and $E_{ion,^{129}\text{Xe}} = 12$ eV [35]. The minimal ionization losses are $\left(\frac{dE}{dx} \right)_{^3\text{He}} = 2$ MeV/g/cm^2 and $\left(\frac{dE}{dx} \right)_{^{129}\text{Xe}} = 1.25$ MeV/g/cm^2, respectively. For a cylindrical target chamber with radius r_{targ} one has $V/L = \pi r_{targ}^2$ where a typical cell has $r_{targ} = 0.8$ cm. Putting everything together one has $\langle \Gamma_{beam} \rangle = 1/(19$ hrs.$)$ for a 15 μA beam on ^{3}He target. For ^{129}Xe target one has $\langle \Gamma_{beam} \rangle = I_b/(4hrs.)$ where I_b is beam current in μA.

The wall relaxation time for a good ^{3}He standard two-chamber cell is no larger than $\Gamma_{wall} < 1/(200 \text{ hrs.})$. Γ_{wall} for ^{129}Xe has been measured previously to be 3.4×10^{-3} s^{-1} for uncoated spherical Pyrex cells with a 3 cm diameter and 0.6×10^{-3} s^{-1} $=1/(1667 \text{ s})$ for silicon-coated Pyrex cells of the same shape and size [33]. Since wall relaxation time dominant factor for Xe polarization, we require coated cells. Also note that the wall relaxation time depends on the ratio of surface to volume. Thus for spherical cell with a radius r one has $\Gamma_{wall}^{-1} = \frac{1.5 \text{ cm}}{r} 3.4 \times 10^{-3}$ s^{-1} and for a cylindrical cell with radius r one has $\Gamma_{wall}^{-1} = \frac{2}{3} \frac{1.5 \text{ cm}}{r} 3.4 \times 10^{-3}$ s^{-1} where $\frac{2}{3}$ comes from the difference in shape. Assuming a cylindrical cell with radius 1 cm, the total relaxation time for Xe is

$$\Gamma^{Xe} = \frac{1}{1667 \text{ s}}(wall) + \frac{I_b}{4 \text{ hrs.}}(beam) \tag{47}$$

Using the spin exchange rate calculated before one has

$$\frac{P_{Xe}}{P_{Rb}} = \frac{1/(20 \text{ s})}{1/(20 \text{ s}) + 1/(1667 \text{ s}) + I_b/(4 \text{ hrs.})} \tag{48}$$

where I_b is again in μA. This gives $\frac{P_{Xe}}{P_{Rb}} \approx 98\%$ at 15 μA and $\approx 96\%$ for 30 μA in the pumping chamber for a Xe fill pressure of 10 atm and a pumping chamber temperature of 120°C.

Similarly the total relaxation time for ^{3}He at 15 μA beam current is

$$\Gamma^{3\text{He}} = \frac{1}{62 \text{ hrs.}}(Dipole) + \frac{1}{200 \text{ hrs.}}(wall) + \frac{1}{19 \text{ hrs.}}(beam) \tag{49}$$

giving $P_{3\text{He}}/\langle P_{Rb}\rangle \approx 54\%$ and $P_{3\text{He},max} \approx 50\%$. Typical ^{3}He polarization during past experiments was about 40% in beam.

A.4 Propagation of the polarized gas to the target cell

A.4.1 Diffusion model for a standard two-chamber cell design

During the finite time it takes for the polarized gas to diffuse from the pumping chamber to the target chamber, the gas depolarizes. Hence, the polarization in the target chamber (P_t) differs from the one in the pumping chamber (P_p). Diffusion model gives the evolution of target polarization in the target and the pumping chamber as [30]

$$\frac{dP_t}{dt} = \frac{A_{Tr} D_t}{V_t L_{Tr}} K(P_p - P_t) + \gamma_{SE}(P_{Rb} - P_p) - \Gamma_p P_p \tag{50}$$

$$\frac{dP_p}{dt} = \frac{A_{Tr} D_t n_t}{V_p L_{Tr} n_p} K(P_p - P_t) - \Gamma_t P_t \tag{51}$$

where D_t the self-diffusion coefficient in the target chamber. Γ_p and Γ_t are the pumping and target chamber spin relaxation rates: $\Gamma_p = \Gamma$ (dipole)+Γ (wall) and $\Gamma_t = \Gamma$ (dipole)+Γ (wall)+Γ (beam). A_{Tr} and L_{Tr} are the cross section and length of the transfer tube as shown in Fig. 10. The target and the pumping chamber densities were given in Eq.(40,41).

For ^{3}He we have the diffusion coefficient $D_{T_0,1 \text{ atm}}^{3\text{He}} = 2.789$ cm^2/s at $T_0 = 80$°C and for any given temperature and pressure one has $D_{T,1 \text{ atm}} = D_{T_0,1 \text{ atm}}(T_t/T_0)^{m-1}$ with $m = 1.7048$ and $D_T = D_{T,1 \text{ atm}} \frac{1 \text{ atm}}{p}$ [30]. Since pressure p is proportional to density at a given temperature we can write $D_T = D_{T,1 \text{ atm}}(0.773 \text{ amg}/[\text{He}])$ where 0.773 amg is the density of 1 atm

gas at a temperature of 80°C. The diffusion coefficient for Xe was measured to be 0.0595 cm^2/s at 1 atm and 343 K (70°C) and is roughly proportional to T [56]. Therefore we use $D_T^{\mathrm{Xe}} \approx 0.0595 \frac{T}{343\ K} (0.773\ \mathrm{amg}/[\mathrm{Xe}])$ cm^2/s. K is a constant coming from the temperature gradient in the transfer tube. For ^{3}He we have $K = (2-m)\frac{1-\frac{T_P}{T_t}}{1-\left(\frac{T_p}{T_t}\right)^{2-m}}$. We assume $K \approx 1$ for ^{129}Xe.

The value of $P_{p,t}$ at equilibrium can be found by forcing $dP_{p,t}/dt = 0$. We obtain:

$$P_p = P_{Rb}\frac{\gamma_{SE}}{\gamma_{SE} + \Gamma_P + G_P \frac{\Gamma_t}{G_t+\Gamma_t}} \tag{52}$$

$$P_t = P_p\frac{G_t}{G_t + \Gamma_t} \tag{53}$$

where

$$G_t = \frac{A_{Tr}D_t}{V_t L_{Tr}} \tag{54}$$

$$G_p = \frac{A_{Tr}D_t n_t}{V_p L_{Tr} n_p} \tag{55}$$

with D_t the diffusion coefficient in the target chamber.

A.4.2 Efficiency of polarization diffusion for standard cell design

In a polarization equilibrium state between the polarization and relaxation effects, P_t and P_p are related by:

$$P_t = \frac{G_t}{\Gamma_t + G_t}P_p \tag{56}$$

The target chamber spin relaxation rate is

$$\Gamma_t = \Gamma\,(dipole) + \Gamma\,(wall) + \Gamma\,(beam) \tag{57}$$

Similarly we have the spin relaxation rate in the pumping chamber

$$\Gamma_p = \Gamma\,(dipole) + \Gamma\,(wall)\,. \tag{58}$$

For the standard cell geometry, $A_{Tr} \approx 1.2$ cm^2, $L_{Tr} = 5.8$ cm, $V_p \approx 110 - 130$ cm^3 and $V_t \approx 80$ cm^3. The ^{3}He densities in the pumping chamber is $n_p \approx 8$ amg and in the target chamber is $n_t \approx 13$ amg. Thus for ^{3}He we usually have $G_t^{^3\mathrm{He}} = 1/(0.55\ \mathrm{hrs.})$. If assuming the same densities n_t and n_p and cell geometries for Xe, we have $G_t^{^{129}\mathrm{Xe}} = 1/(27\ \mathrm{hrs.})$. Using the dipole, wall and beam spin destruction rates described in the previous section we find $\Gamma_t^{^3\mathrm{He}} \approx 1/(13.6\ \mathrm{hrs.})$ for 15 μA beam and $\Gamma_t^{^{129}\mathrm{Xe}} \approx 1/(0.106\ \mathrm{hrs.})$. Hence, for ^{3}He we have $P_t = \frac{1/0.55}{1/0.55+1/13.6} = 0.96 P_p$. For Xe we have $P_t = \frac{1/27}{1/27+1/0.106} = 0.004 P_p$. This implies that a new cell geometry is needed in order to achieve reasonable polarization of Xe in the target chamber.

35

B Radiative Corrections for g_1

Radiative corrections to doubly polarized lepton-nucleon scattering are well know [59]. Furthermore, assuming:

- a negligible contribution from coherent reactions (typically the elastic tail),

- the same radiation lengths for the ^{3}He and Xe targets,

- no significant Coulomb correction in the case of the Xe,

- no EMC effect,

then the radiative correction should be the same for g_1^{He} and g_1^{Xe} since unpolarized material cancels in the polarized cross section used to extract the spin structure functions. Under these assumption, the radiative corrections cancel each other in the EMC ratio and no uncertainty from the radiative corrections should be expected. The pertinence of the above assumptions will now be discussed.

B.1 Contribution from elastic tail

At 6 GeV, the elastic tails are generally suppressed. However, when the scattering is from a high Z target with form factors fast rising with $1/Q^2$, this statement needs to be verified.

Typical radiation lengths of the polarized ^3He target are 0.17% before scattering and 3% after (for 13.5^o scattering). 20 cm of Xe at 1.7 amg and room temperature adds a radiation length of 2.2% before scattering. The elastic tail of unpolarized cross section at the kinematics of our experiment

Figure 11: Unpolarized cross sections for $e-$Xe elastic scattering tail compared to inelastic scattering at the proposed kinematics. The two vertical lines show the range in ν for scattered electrons detected by the HRS.
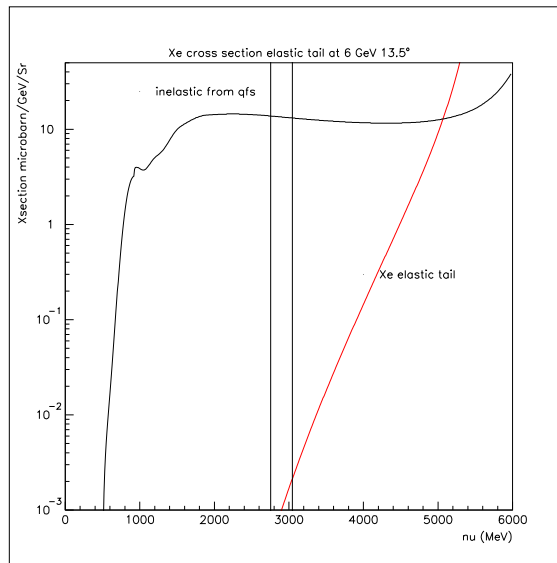
($E = 6.0$ GeV, $E' = 3.10$ GeV, $\theta = 13.5°$) is shown in Fig 11 for 3% in and out radiation length, along with the inelastic cross section calculated using the QFS code [60]. The kinematics of our experiment is shown by the two vertical bands. We conclude from this result that correction from elastic scattering, and presumably from all other coherent reactions, is negligible.

B.2   Difference in radiation lengths

Since the target cells are hand-made, the Xe and He cells will not be exactly the same. Some difference in window and wall thicknesses will exists. Typically, window thicknesses vary from 100 to 150 μm. Wall thicknesses, for walls made of the same glass material, will typically vary by less than 10%. Furthermore, as discussed in the previous section, filling a cell with Xe will add 2.2% radiation length (the corresponding radiation length for a He cell is negligible).

The window thicknesses and Xe pressure will be known before the experiment. Hence, the difference of radiation lengths on the incoming electron path between a Xe cell and a He cell can be easily cancelled by adding some material during the He runs. For example material can be added on the beam pipe vacuum window. Similarly, the radiation lengths on the outgoing electron path can be made equal by adding material on the aluminum exit window of the scattering chamber. All in all, it is not a problem to equalize the radiation lengths of the He and Xe setups.

B.3   Multi-photon corrections

B.3.1   Soft photons (Coulomb correction)

Multi-photon exchange is more important in the case of Xe due to its much larger Z. At low incoming beam energy ($\sim$ GeV), this can be accounted at first order in the case of soft photons by the approximation of the effective moment. At 6 GeV, it can be used to indicate the importance of the effect.

This technique can be easily explained: the incoming electron is accelerated as it enters the positively charged Coulomb field of the Xe nucleus, large compared to the one of He. It is then decelerated after its scattering off the Xe nucleus. All in all the effect can be accounted of by shifting the incoming and outgoing energies of the electron by $-V_0$, the coulombian potential for Xe. We have $V_0 = -18.6$ MeV.

For the Xe case, the nominal kinematics is:

- E=6.0 GeV, $\nu = 2.9$ GeV ,Q^2 =1.0278 GeV^2, x =0.1889 .

It will change to

- E_{eff}=6.018 GeV, $\nu_{eff} = 2.9$ GeV, $Q^2_{eff} = 1.0309$ GeV^2, $x_{eff} = 0.1883$.

The kinematics change is thus very small (0.3% for Q^2 and x). We conclude from this first order calculation that the Coulomb correction is negligible in the case of this experiment.

B.3.2   Hard photons (two photon exchange)

The magnitude of the correction should be the same as for the free nucleon case since the quarks are resolved by the hard photons. Consequently, it should be negligible, as for the free nucleons case in the DIS regime, and there is no special issue with dealing with a high-Z nucleus.

B.3.3   Intermediate case

We also have the intermediate case of a hard photon coupling to a quark while a softer photon couples to the nucleus. Since the two limiting cases (Coulomb correction and two photon exchange) are small effects, we may expect this effect to be small too. Furthermore, two-photon exchange corrections are suppressed at forward angles due to the dominance of the one-photon $1/Q$ propagator. We will detect electrons at 13.5^o. Consequently, we do not expect significant corrections.

B.4   EMC effects

At a given kinematic and given radiation lengths, radiative correction effects depend on the value of the polarized cross section. Hence, a change in $g_{1,2}$ due to nuclear modification will yield different radiative corrections.

The effect of radiative corrections on the difference of polarized cross sections in the case of a longitudinally polarized target, $\Delta\sigma_{\|}$, has been calculated in Ref. [36] for a setup and a kinematics similar to our proposed measurement ($Q^2 = 1.13\,\mathrm{GeV}^2$ and $x = 0.19$). It is found that $\Delta\sigma_{\|,born} = \Delta\sigma_{\|,meas}(1 - \delta)$, with $\delta = 4.5\%$ for the value of $g_{1,2}$ of a free neutron. Assuming (arbitrarily for now) a linear dependence of δ with the spin structure functions and a 20% modification of those due to the nuclear medium, the net effect of the radiative corrections on the EMC ratio will be 0.9%. Taking a 7% uncertainty as used in Ref. [36], the uncertainty on the radiative corrections due to the EMC effect is 0.06%.

B.5   Conclusion

The effects that would cause radiative corrections to be different in the cases of He and Xe turn out to be small. All in all, we expect a negligible uncertainty on the EMC ratio due to the radiative corrections.

References

[1] European Muon Collab, J. Aubert *et al.*, Phys. Lett. **B123**, 275 (1983).

[2] M.R. Adams *et al.* (FermiLab E665 Collaboration), Phys. Rev. Lett. **68**, 3266 (1992).

[3] J. Arrington *et al.*, Jefferson Lab E03-107, A Precision Meausurement of the Nuclear Dependence of Structure Functions in Light Nuclei, data analysis in progress.

[4] D.F. Geesaman, K. Saito and A.W. Thomas, Annu. Rev. Nucl. Part. Sci. **45**, 337 (1995).

[5] I. Sick and D. Day, Phys. Lett. **B274**, 16 (1992).

[6] F.E. Close, R.G. Roberts and G.G. Ross, Nucl. Phys. **B296**, 582 (1988).

[7] L. Frankfurt, V. Guzey and M. Strikman, Phys. Lett. **B381**, 379 (1996).

[8] V. Guzey and M. Strikman, Phys. Rev. C **61**, 014002 (2000).

[9] I.C. Cloët, W. Bentz and A.W. Thomas, Phys. Rev. Lett.**95**, 052302 (2005).

[10] J.R. Smith and G.A. Miller, Phys. Rev. C **72**, 022203 (R) (2005).

[11] E. Leader, A.V. Sidorov and D.B. Stamenov, Eur. Phys. J. **C23**, 479 (2002), arXiv: hep-ph/0111267

[12] J. Bluemlein and H. Boettcher Nucl. Phys. **B636**, 225 (2002), arXiv: hep-ph/0203155.

[13] M. Hirai, S. Kumano and N. Saito (Asymmetry Analysis Collaboration), Phys. Rev. D **69** 054021 (2004), arXiv: hep-ph/0312112

[14] A.D. Martin, R.G. Roberts, W.J. Stirling and R.S. Thorne, Eur. Phys. J. **C28**, 455 (2003), arXiv: hep-ph/0211080.

[15] S. Wandzura and F. Wilczek, Phys. Lett. B, **72**, 195 (1977).

[16] J. Alcorn *et al.*, Nucl. Instrum. Meth. A **522**, 294 (2004).

[17] R. Michaels, P.E. Reimer, X. Zheng *et al.*, Jefferson Lab E05-007, Polarized e-2H Parity Violating Deep Inelastic Scattering at CEBAF 6 GeV.

[18] R. Michaels, P. Souder, G. Urciuoli *et al.*, Jefferson Lab E03-011, Neutron Skin of 208Pb through Parity Violating Electron Scattering.

[19] B. Humensky, *General exam advanced project*, Princeton University (1999); B. Humensky, *Ph.D. Thesis*, Princeton University (2003).

[20] HAPPEX-He (E00-114) and HAPPEX-H (E99-115) 2005 runs, http://hallaweb.jlab.org/experiment/HAPPEX/

[21] N. Liyanage, *Spectrometer constant determination for the Hall-A High Resolution Spectrometer Pair*, Jefferson Lab Hall A technote, JLAB-TN-01-049.

[22] H. Ibrahim, P. Ulmer, N. Liyanage, JLAB Hall A Technical Notes JLAB-TN-02-032, (2002).

[23] X. Zheng, *JLAB Hall A detector PID efficiency analysis using high electron and high pion rate data*, see E99-117 website http://hallaweb.jlab.org/physics/experiments/he3/A1n/

[24] A. Brown, priv. communication.

[25] A. Poves, priv. communication.

[26] I.A. Nelson, B. Chann and T.G. Walker, Appl. Phys. Lett. **76**, 1356 (2000).

[27] B. Chann, I. Nelson and T.G. Walker, Opt. Lett **25**, 1352 (2000).

[28] B. Chann, E. Babcock, L.W. Anderson *et al.*, J. Appl. Phys. **94**, 6908 (2003).

[29] F.J. Adrian, Phys. Rev. **138**, A403 (1965).

[30] M.V. Romalis, Ph.D. thesis, Princeton University, 1997

[31] T. Walker, Phys. Rev. A 40, 4959 (1989).

[32] T. Chupp *et al.*, Phys. Rev. A **38**, 3998 (1988).

[33] X. Zeng *et al.*, Phys. Rev. A **31**, 260 (1985).

[34] hyperphysics.phy-astr.gsu.edu/hbase/chemical/ionize.html

[35] Particle Data Group 2005, http://pdg.lbl.gov/2005/reviews/contents_sports.html

[36] K. Kramer, Ph. D thesis, College of Willam and Mary, 2003.

[37] W. Happer, G.D. Cates, M.V. Romalis and C.J. Erickson, U.S. Patent No.6 318092 (2001).

[38] E. Babcock, I. Nelson, S. Kadlecek *et al.*, Phys. Rev. Lett. 91, 123003 (2003).

[39] JLab E97-110 Techical Note #4: A. Deur, "Two Step Process for the Rising Tail Background", 03/31/2003; URL: http://hallaweb.jlab.org/experiment/E97-110/tech/tech_notes.html.

[40] R. L. Jaffe, in *Relativistic Dynamics and Quark-Nuclear Physics*, M. B. Johnson and A. Picklesiner (Eds.), Wiley, New York, 1986.

[41] C. Ciofi degli Atti *et al.*, *Phys. Rev.* **C48**, R968 (1993).

[42] F. Bissey *et al.*, *Phys. Rev.* **C64**, 024004 (2001).

[43] F. Bissey *et al.*, *Phys.Rev.* **C65**, 064317 (2002).

[44] A. Nogga, Ph. D. thesis, Ruhr-Universität Bochum, Bochum, Germany, 2001.

[45] X. Zheng, Ph.D. Thesis, Massachusetts Institute of Technology, 2002.

[46] E. Caurier *et al.*, Rev. Mod. Phys. **77**, 427 (2005)

[47] JLab E05-012, S. Gilad, D. Higinbotham, W. Korsch, B. Norum and S. Sirca, *et al.*, Measurements of A_x and A_z Asymmetries in the Quasi-elastic ^{3}He$(e, e'd)$ Reaction.

[48] D. E. Wiser, *Ph.D. thesis*, Univ. of Wisconsin, (1977);

[49] M. Arneodo *et al.*, Phys. Lett. B **364**, 107 (1995).

[50] K. Kramer *et al.*, Phys. Rev. Lett. **95**, 142002 (2005).

[51] T.G. Walker and W. happer, Rev. Mod. Phys. **69**, 2 (1997).

[52] I. Kominis, Ph.D. thesis Princeton University, 2001

[53] G.D. Cates, R.J. Fitzgerald, A.S. Barton et al., Phys. Rev. A **45**, 4631 (1992)

[54] T.J. Killian, Phys. Rev. **27**, 578 (1926).

[55] K.D. Bonin, D.P. Saltzberg and W. Happer, Phys. Rev. A, **38**, 4481 (1988).

[56] P.W.E. Peereboom, H. Luigjes and K.O. Prins, Physica A, **156**, 260 (1989).

[57] W. Xu, Ph.D. Thesis, Massachusetts Institute of Technology, 2002.

[58] W. Xu *et al.*, Phys. Rev. C **67**, 012201, (2003).

[59] Akushevich *et al.*, J. Phys. G **20**, 513 (1994).

[60] (QFS code) J. W. Lightbody, Jr., J. S. O'Connell, Computers in Physics, May/June (1988);